AN EXPLORATION OF SEVERAL STRUCTURAL MEASUREMENT TECHNIQUES FOR USAGE WITH FUNCTIONALLY GRADED MATERIALS

THESIS

Robert Reuter

AFIT/GAE/ENY/07-D03

DEPARTMENT OF THE AIR FORCE
AIR UNIVERSITY

AIR FORCE INSTITUTE OF TECHNOLOGY

Wright-Patterson Air Force Base, Ohio

The views expressed in this thesis are those of the author and do not reflect the official policy or position of the United States of America, Department of Defense, or the United States Government.

AFIT/GAE/ENY/07-D03

AN EXPLORATION OF SEVERAL STRUCTURAL MEASUREMENT TECHNIQUES FOR USAGE WITH FUNCTIONALLY GRADED MATERIALS

THESIS

Presented to the Faculty

Department of Aeronautics and Astronautics

Graduate School of Engineering and Management

Air Force Institute of Technology

Air University

Air Education and Training Command

In Partial Fulfillment of the Requirements for the

Degree of Master of Science in Aeronautical Engineering

Robert A. Reuter, BS

December 2006

AFIT/GAE/ENY/07-D03

AN EXPLORATION OF SEVERAL STRUCTURAL MEASUREMENT TECHNIQUES FOR USAGE WITH FUNCTIONALLY GRADED MATERIALS

Robert Reuter, BS

Approved:

Marina Ruggles-Wrenn (Chairman)	date
Anthony Palazotto (Member)	date
Thomas Eason (Member)	date

AFIT/GAE/ENY/07-D03

Abstract

Titanium / titanium boride functionally graded 6”x1”x1” beams were subjected to a four-point beam test in order to critique the value of several measurement techniques. Also, finite element analysis results were compared with experimental values and general observations about the experiment were recorded. Uniform 85% TiB / 15% Ti and uniform commercially pure titanium specimens were also subjected to the same loading conditions as a control. Techniques used include digital image correlation, fiber optic strain gauging, strain gauging, and differential infrared thermography techniques. The strain data results were compared with one another and to linear finite element models. It was found that several of the techniques had distinct advantages and disadvantages for usage in a layered functionally graded system. Furthermore, the finite element showed good agreement with results when overlaid with several of the measurement techniques.

To my wife

Acknowledgements

I would like to convey my appreciation to those who helped to facilitate my thesis work. First and foremost, I would like to express gratitude to my beautiful wife, for her sacrifice in allowing me to complete my studies. I would also like to acknowledge Dr. Marina Ruggles-Wrenn for her guiding hand, Dr. Eric Tuegel for his assistance in acquiring the funding necessary for the project and his constant guidance, Maj. Jim Rogers for giving me the opportunity to juggle work and school, Dr. Kristina Langer for continuing Jim's vision, Capt. Glenn Cooley, Dr. Tom Eason, Thomas Tuegel, and Mr. Jeff Quast. Furthermore, I would like to thank the leadership of AFRL/VA for setting up the programs which enabled me to succeed.

Robert A. Reuter

Table of Contents

List of Figures

AN EXPLORATION OF SEVERAL STRUCTURAL MEASUREMENT TECHNIQUES FOR USAGE WITH FUNCTIONALLY GRADED MATERIALS

INTRODUCTION

1.1 Background

Functionally graded materials (FGM) are an unexplored frontier in research in that countless permutations of materials can be combined to form a myriad of new material systems. Much computational work regarding FGMs has been performed. For example, Erdogan and Chiu created a continuum model to solve buckling instability problems for FGMs. [Erdogan, 1996] Gu and Asara proposed a model to measure crack deflection for brittle functionally graded materials and found that material grading has a lesser effect around material boundaries. [Gu, 1997] Reddy analyzed the differences in deflections and stresses using a nonlinear finite element. Material gradients were approximated using a power law approximation.[Reddy, 2000] Work regarding free and forced vibrations by Yang and Shen found that at elevated temperatures, when considering FGMs in relation to an isotropic substance, FGMs do not necessarily have intermediate natural and dynamic responses. [Yang, 2000].

In most instances, little laboratory testing has been performed to validate predictive FGM models. However, some examples do exist. Rodriguez-Castro et. al., tested the microstructure and mechanical behavior of Al A359/SiCp. Tensile and fracture properties and SEM micrographs were gathered to characterize the system. [Rodriguez-Castro, 2002] Atri, Ravichandran, and Jha used an impulse method to measure elastic properties through vibration. [Atri, 1999] From their work, they determined that a

titanium-titanium monoboride-titanium dirboride system displayed increased modulus properties from that of the standard titanium.

The most similar study involving the Ti-TiB material system to this work was performed by Ma and Tan measuring the flexural strength and fracture toughness of the material. Although Ma and Tan's work is closely related, many differences exist. Fundamentally, Ma and Tan used only 5 mm (0.196 inches) thick beams while in this study 25.4 mm (1.0 inches) were analyzed. Ma and Tan were also more interested in the processing and characterization of the functionally graded system. They studied the effect of the particle size on sintering, the effect of the silicon carbide additive on the densification of the titanium diboride rich layer, and the effect of the particle size and additive on the mechanical performance of the functionally graded material. [Ma, 2001]

In contrast to Ma and Tan's work, the main purpose of this investigation is less about understanding the material behavior of the material system and more about determining the strengths and weaknesses of several novel measurement techniques for usage with a complex composite system – in this case, a functionally graded material. However, general failure observations about the structure and comparison with finite element analysis were also performed because of the uniqueness of the material system. Another benefit of the finite element analysis was that they were used as a baseline for use in conjunction the experimental results.

The four-point bend was chosen as the mechanism to observe the mechanical behavior of an FGM system. The Ti-TiB material system was chosen because the work performed was part of a larger effort to study the material system for possible usage in quick turn-around hypersonic vehicles and other extreme thermo-acoustic environments.

1.2 Motivation

As part of the United States' Air Force's vision to establish global vigilance, reach, and power, the Air Force Research Laboratory (AFRL) must help meet the warfighter's needs – both current and projected. This effort is in part a building block to provide the warfighter with a 'war-winning technology' and in part a project to spawn other research topics.

The main idea of using FGMs over conventional materials is that the internal composition can be catered to meet the requirements of any given system. Although much of this technology has not been fully proven, the internal structure of the material could be laid out to form complex electrical circuits, hybrid high temperature pressure vessels, or thermal structures. However, before complicated applications are fabricated out of FGMs, it is imperative that rudimentary structural questions be answered before commencing with larger scale use. This work is just one step in being able to properly design using a functionally graded material system.

On a grander scale, the ultimate goal of this research is to help determine if the titanium / titanium boride system can be used within the context of the structure of a reusable, hypersonic launch vehicle. In the case of the space shuttle, the aluminum substructure is shielded by a thermal protection system (TPS) barrier consisting of several layers of primers, tile, adhesives, fibers, and coatings. The main advantage of using and FGM configuration would be that the underlying metallic structure could possibly withstand higher temperatures and reduce TPS size requirements. Also, weight could be further minimized by tailoring the constituent makeup of each component based upon the load and stress interactions present in different areas of the spacecraft.

1.3 Outline

This section provides an overview of the preceding chapters. Chapter II gives an overview of basic bending theory, finite element analysis, and other measurement techniques. Chapter III provides the details of the experimentation. Chapter IV lists the results of the tests and analyzes any significant findings. Chapter V concludes the thesis and discusses and future work created from the experimentation.

THEORETICAL AND EXPERIMENTAL BACKGROUND

2.1 Basic Bending Theory

The well-known Euler-Bernoulli beam equation for the normal stress can be determined along any distance y from the neutral axis:

$\sigma_{xx} = - My/ I$

σ_{xx} = stress
M = moment
y = distance from neutral axis
I = second moment of inertia

From this basic relationship, combined with the shear and moment diagram from an idealized four point-bend, a simple approximation of the stresses for a beam structure can be determined.

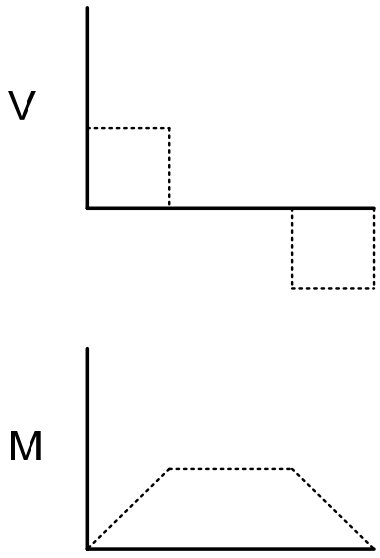

Figure 1: Shear and moment diagram of 4-point bend specimen

From this simple analysis, accurate stress results for the experimental setup cannot be established; however, general bending behavior for the four-point bend

configuration can be roughly identified. When looking at the region perpendicular to loading along the at the top and bottom surfaces, it is anticipated that one side of the beam will be subjected in compression and the opposite will be in tension. Furthermore, a region of varying moment exists in the zones between where the opposing loads are applied. Finally, a zone of constant moment exists in the medial region.

2.2 Finite Element Analysis Approach

Finite element uses a geometrically similar model containing multiple, linked, and simplified representations of discrete regions. Theories of elasticity are invoked where equations of equilibrium, compatibility relationships, and constitutive relationships are applied to each element, and a system of simultaneous equations is created. These equations are then solved for unknown values using linear algebra techniques. In a structural analysis, unknown values typically include stresses, strains, and displacements.

Because of the low expense and excellent reputation of numerical modeling, finite element analysis (FEA) was chosen as a foundation for comparison with the functionally graded system in 4-point bend. Also, FEA can extract information on the entire structure, whether internal or external. This is particularly important because most of the laboratory measurement techniques are bound to only the surface, particularly with the chosen geometry in this experiment.

There are also many drawbacks to this type of analysis. First, when modeling, several assumptions have to be made regarding the boundary conditions and material makeup. In the real four-point bend test, the loading does not occur in a completely uniform pattern; therefore, when interpreting FEA results around the geometry roller errors could be quite high. In a functionally graded material, the material properties assigned to the structure can create a large discrepancy between the modeling and laboratory acquired data. During this work, the properties were assumed to be instantaneously transitioned because the system was originally assembled in seven discrete layers when fabricated by the manufacturer. However, in a more complicated graded FGM system, this assumption would not necessarily suffice.

2.3 Measurement Techniques

2.3.1 Strain Gages

Strain gages have two common purposes: determining the state of strain at an averaged point in order to determine stress or to act as a strain-sensitive transducer element. In this work, the first of the two uses was utilized. The theory of operation of the strain gages works on the premise that when the length of the foil of the gage is increased the electrical resistance is also increased. When combining this relationship with the null-balance condition and Ohm's law from the voltage-sensitive Wheatstone bridge, the desired unknown strain quantity can be determined.

2.3.2 Fiber Optic Strain Gages

Each fiber uses several Fiber Bragg Gratings (FBGs), a device created by etching the core of the fiber with a laser. When laser light is passed through the fiber, each grating reflects back only certain wavelengths. When in the presence of mechanical changes, these reflections are modified and can therefore be used to indirectly measure strain. Gratings in each fiber are spaced at a frequency of ten millimeters. The total length of each FBG is approximately six millimeters in length. This region is the area averaged by each sensor. Furthermore, the system is only capable of picking up changes relative to the lengthwise direction of the fiber.

Fibers were attached to the surface of each specimen using a common adhesive. Therefore, some error is induced because when interpreting results the strain is assumed to be measured at the surface of the metallic structure and not on the outer skin.

2.3.3 Digital Image Correlation

Digital image correlation (DIC) or the white light speckle technique is an optical-numerical method used to take full-field strain and displacement and strain measurements of the surface. The digital in the DIC system uses a silicon grid of individual light sensitive cell or pixels to acquire light intensities reflected back from the desired surface. Then, two images of the specimen at different states, deformed and undeformed, are compared by searching for a subset of the undeformed image in the deformed image in order to maximize a given similarity function. The displacement result is an average of the displacements of the pixels inside each subset. These displacements can then be calculated into strain measurements.

Digital image correlation can be used with a fair amount of ease in order to achieve reasonable results when in two-dimension. However, three-dimensional usage of the system is more complicated as the extra dimension adds another layer of complexity to the image recognition routines and the numerical algorithms necessary to properly measure displacements to determine strains. It has also been seen that the speckle pattern on a specimen will adversely affect the results on a specimen if not properly sized and distributed. [Lecompte, 2006] Although speckling could be a factor when using digital image correlation, the speckle pattern was not optimized during the course of

experimentation because the initial results yielded good agreement with analytical models without further tweaking.

2.3.4 Differential Infrared Thermography

Any substance becomes slightly warmer or cooler when acted upon by a force. If the substance is changed by a tensile force the substance becomes slightly cooler and vice versa. This phenomenon is known as the thermoelastic effect.

The equation which describes the thermoelastic effect is as follows:

$$\Delta T = - \alpha * T / \rho / C_p * (\Delta\sigma_x + \Delta\sigma_y)$$

α = coefficient of thermal expansion
T = absolute temperature
ρ = density
Cp = specific heat
$\Delta\sigma_x$, $\Delta\sigma_y$ = stress amplitude

In other words, if a minute change in temperature which caused the thermoelastic effect is detected, the change in the addition of ‘x’ and ‘y’ direction stresses can be determined.

Thermoelastic stress analysis is the term used to describe the mapping over a surface of a structure of the temperature amplitude over a varying load using an infrared camera. As a means to better the measurements, the readings are time averaged with continuous dynamic loading. When mapping, the differing colors correspond to different amounts of thermal change and thus varying values of surface stress.

Differential infrared thermography is an excellent technique for viewing stresses in a four-point bend configuration in that it yields high resolution, statistically accurate images when properly acquired. However, this imaging technique is not without its

shortcomings. When acquiring images, the system requires the room temperature to remain at a fairly constant level and background interference to be relatively minimal. The system can detect small temperature variations on the order to 0.05°C. Therefore, it would be very difficult to use this system in most natural environments. Adequate acquisition time must also be considered when running the tests. Originally, the samples were run for only seven seconds of acquisition time and yielded poor, 'fuzzy' results. When this time was changed to three minutes, much cleared images were acquired. Another drawback of the system is the usage of liquid nitrogen necessary for the sensor array. If liquid nitrogen is not properly refreshed at the appropriate intervals, images can become blurred. As an alternative, other commercial systems are available which use a compressor to cool the sensor array instead of the liquid nitrogen.

Differential infrared thermography also has limitations on the field data it can acquire during testing. For example, edge effects were present. These effects were caused by the detection of surfaces heat irradiating from the bend specimen and the discrepancy between the specimen and the background. This effect is present in the thermography photos depicted in Section 4.4. Although the software has a corrective tool to help lessen these effects, these anomalies still add another element of error to the approximation of stresses. This is problem more problematic when the area of interest lies directly on the boundary such as in the case of a crack.

When dealing with functionally gradient materials, this technique is not ideal because a strain gage is required to determine the reference stress value in a region of constant stress and modulus. Since the FGM is a non-homogenous structure, in many instances, no good region will exist to lay down a strain gage and determine the

multiplier necessary to convert data from pixel units into stress. Technically, a gage can be put down to estimate the strain over a region; however, the amount of error created from this mismatch would have been very difficult to properly differentiate.

Finally, since the thermographic technique can only detect the addition of the stresses in two directions perpendicular to the camera's focal direction, it is difficult to differential the 'x' and 'y' direction stresses in most bi-axial and tri-axial configurations without any outside information. In this work, this limitation is particularly problematic because the thermography system cannot be directly compared to the other strain and displacement measurement devices.

2.4 General Fracture Behavior of Metals and Ceramics

In a ceramic fracture, the beginning of the crack propagation can be traced to the fracture origin, the area of the strength-reducing flaw which initiated failure. The next prominent region which surrounds the fracture origin is the fracture mirror, an area whose unevenness and surface roughness are much lower than the remaining surface. However, depending on the material and loading condition this morphology may vary. A higher fracture stress can cause the fracture mirror to completely disappear. If the stresses were to decrease due to decrease in external load or crack branching, the surface may again appear smooth. On the other hand, if the crack entirely propagates under lower stresses, the whole surface may appear relatively smooth. [Mencik, 1992]

In metallic structures, four principal fracture modes exist: dimple rupture, cleavage, fatigue, and decohesive rupture. Dimple fracture typically happens under a single load or tearing in which depressions or dimples in the microstructure occur from microvoids. Depending upon the loading conditions, the microstructure will exhibit a unique dimple pattern. Transgranular cleavage occurs at well defined planes in which the crystal structure is either body centered cubic (bcc) or hexagonal closed packed (hcp). The mode results from triaxial stresses at a high rate of deformation and at lower temperatures. Fatigue failure is typically detected by striations on the crack face. Finally, decohesive rupture is present along weak material surfaces such as grain-boundary precipitation, low-strength phases, defect structure, hydrogen embrittlement, and stress-corrosion cracking. [ASTM, 2001]

TEST PROCEDURE

3.1 Description of Specimens

3.1.1 Specimen Fabrication and Acquisition

The functionally graded Ti/TiB specimens were acquired from Cercom, Inc of Vista, CA. Despite the relatively simple geometry, Cercom was contracted to manufactur the final rectangular specimen because of unknown intricacies involved with machining Ti/TiB FGMs. Along with the FGM specimens, cp Ti and 15% Ti/ 85% TiB were included along with the first shipment from the company. The 15% Ti / 85% TiB layering was chosen by the manufacturer as the maximum allowable amount of TiB. Due to the damage of the pure Ti/TiB caused by ceramic composite brittleness, five new specimens had to be fabricated over and reshipped. Specimens were fabricated at Cercom using a hot-isostatic pressing process (HIP).

3.1.2 Physical Description

On the sides of each specimen, the individual material layers can be seen with the naked eye showing the layed gradation. From the naked eye, differentiating the titanium and titanium boride layers was sometimes difficult as the color of the two materials was fairly close. Also, the coloring between layers did not necessarily reflect back a predictable color. In other words, in certain light, the shading in the middle appeared

darker than either of the other top and bottom layers.

Figure 2: Side profile of Ti/TiB specimen

3.1.3 Specimen Design

The dimensions of each specimen are nominally 1”x 1”x 6”. Thicker specimens were opted over more conventional, thinner, bending specimens for two primary reasons. The thicker specimens allowed for the geometric nonlinearities of the loading to be neglected. In addition, by having thicker layers, layering errors would become less significant so that the modeling results would be more accurate.

The functionally gradient materials were created with the following layer stacking sequence:

Layer#	***% TiB***	***Thickness (in)***
1	85	0.125
2	75	0.125
3	60	0.125
4	45	0.125
5	30	0.125
6	15	0.125
7	0 (pure Ti)	0.25

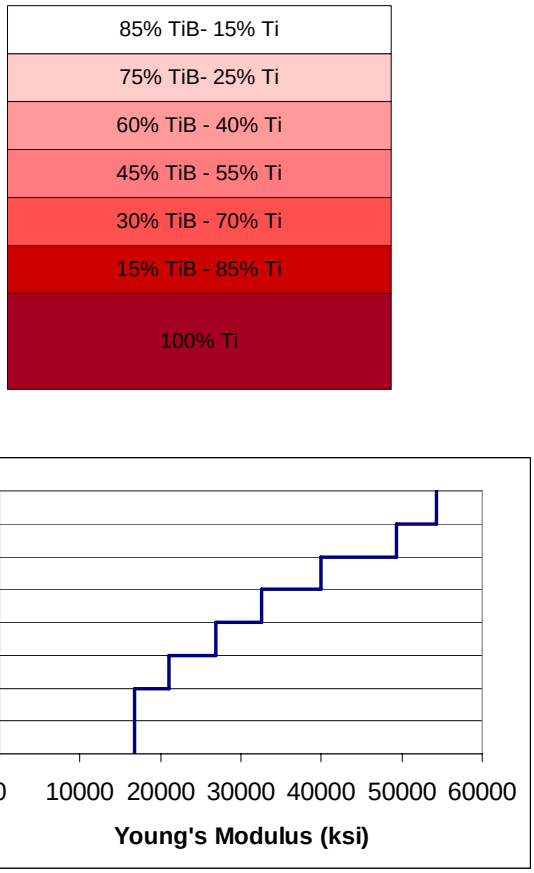

Figure 3: Pictorial representation of Ti/TiB layering and Young's Modulus Distribution

3.2 On ASTM Standards for Bending Tests

Because the material system is unique to the applicable testing procedures, no one unique standard could be followed. Furthermore, the specimen design was determined prior to evaluating each standard and does not necessarily follow any one set of guidelines. Closely applicable standards include: ASTM D 790, 'Standard Test Methods for Flexural Properties of Unreinforced and Reinforced Plastics and Insulating Materials'; ASTM E 290, 'Standard Test Methods for Bend Testing of Material for Ductility'; and ASTM D 6272 'Standard Test Method for Flexural Properties of Unreinforced and Reinforced Plastics and Electrical Insulating Materials by Four-Point Bending'. Deviations from the standards included specimen geometry, test setup, and loading conditions. Furthermore, no guidelines were present in order to handle metallic-ceramic composite structures.

3.3 Equipment and Setup

3.3.1 Experimental Setup and Equipment

For digital image correlation, a Correlated Solutions® digital image correlation system was connected to a personal computer loaded with Vic-Snap and Vic-2D [Figure 4: A, B], the company's correlation software. In the case of differential infrared thermography, the DeltaTherm® system by Stress Photonics® was used to acquire stress field images. [Figure 4: B] The strain gages were attached to a National Instruments' SCXI-1000 system. [Figure 4: C] When running fiber optic strain gage tests, the Luna Innovations Distributed Sensing System® was attached to a one-meter fiber. (Fiber ID: 001.0-B-001.0-0.01-46-SP) [Figure 4: D]

As a means to bend the Ti/TiB specimens, an MTS test frame was used. In the test frame, an MTS 609 Alignment Fixture is used to grip the bending test fixture. The Sintech 20/D machine is controlled by Testworks for Windows: Version 3.02. [Figure 4: C]

The three / four point bending test fixture was purchased from Wyoming Test Fixtures and was designed to the specifications of ASTM D790 and D6272. [Figure 4: E] The fixture is shown in Figure 5 with a specimen prepared for digital image correlation. Although these specifications are not fabricated specifically for functionally graded materials, the fixture was used because no better alternative existed.

Finally, an external halogen light source was used to enhance the quality of digital image correlation results. [Figure 4: F]

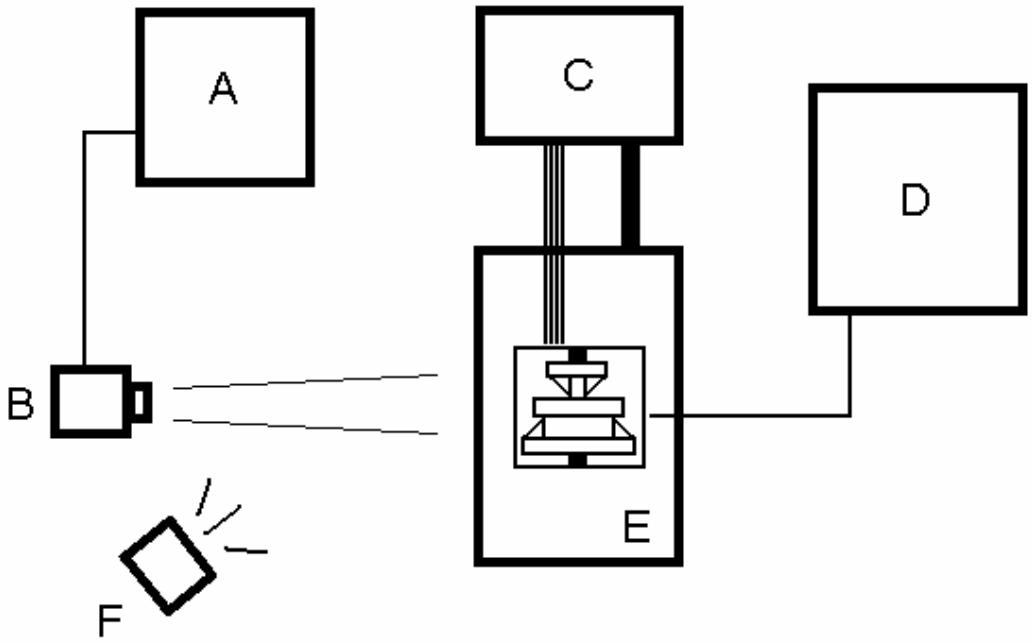

Figure 4: Diagram of experimental setup

A: Test Computer

B: Digital Image Correlation or Differential Infrared Thermography Camera

C: Test Computer, Controller and Strain Gage Acquisition System

D: Fiber Optic Strain Gage System

E: Test Frame, 4-Point Bend Fixture, and Specimen

F: External Halogen Light Source (DIC only)

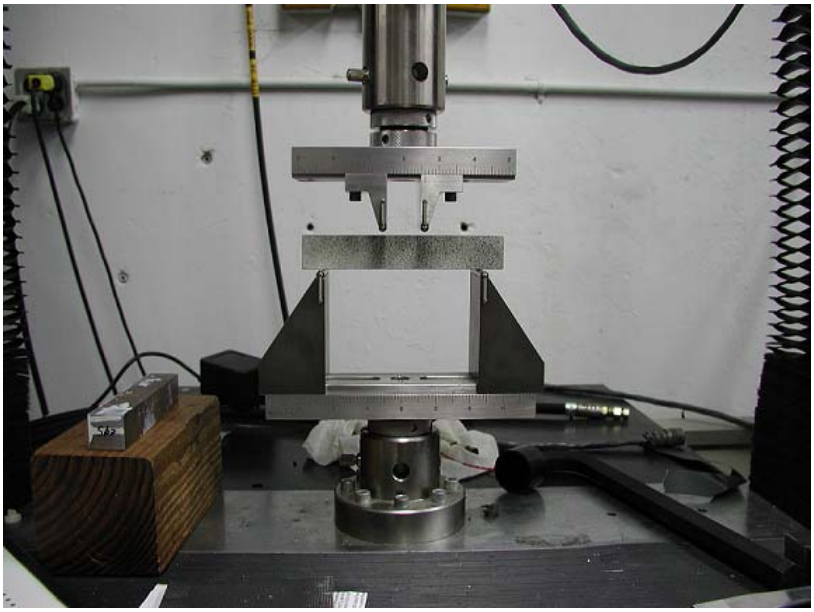

Figure 5: Four point bend fixture with 6”x1”x1” specimen prepared for DIC

3.3.2 Specimen Preparation

Before testing began, each specimen was prepared to accommodate electrical resistance strain gages, a fiber optic gage, and digital image correlation. On the top surface, the area in compression, two uniaxial gages were laid to detect the 'x' direction stresses. On the bottom surface, the area in tension, a single rosette was laid to determine both the 'x' direction stresses but also any rotational misalignment. Uniaxial and rosette gages had a gage length of 0.125", a gage factor of 2.11 and a grid resistance of 350Ω. (MM CEA-06-125-UN-350; MM CEA-06-125-UR-350) Because a strain gage would span over differing material regions, the decision was made to omit strain gages from the front and back surfaces to allow room for other measurement techniques. When laying strain gages, standard protocol was followed including sanding, degreasing, conditioning, neutralizing, curing, and soldering. In both cases, a cyanoacrylate adhesive was used to secure the strain gages to the specimen.

Due to the strain algorithm utilized by the digital image correlation system, the front each specimen was coated with a thin coating of white latex paint and then speckled with black latex paint on the front surface. For specimens using differential infrared thermography, a matte, black finished was applied to the front. Finally, in the case of the fiber optic gages (LUNA 001.0-B-001.0-0.01-46-SP), horizontal lines were inscribed on the back surface at a location 1/8" from the top surface, in the middle, and 1/8" from the bottom surface. Again, a cyanoacrylate adhesive was used to secure the gages.

Figure 6 summarizes the preparation required for each data acquisition technique.

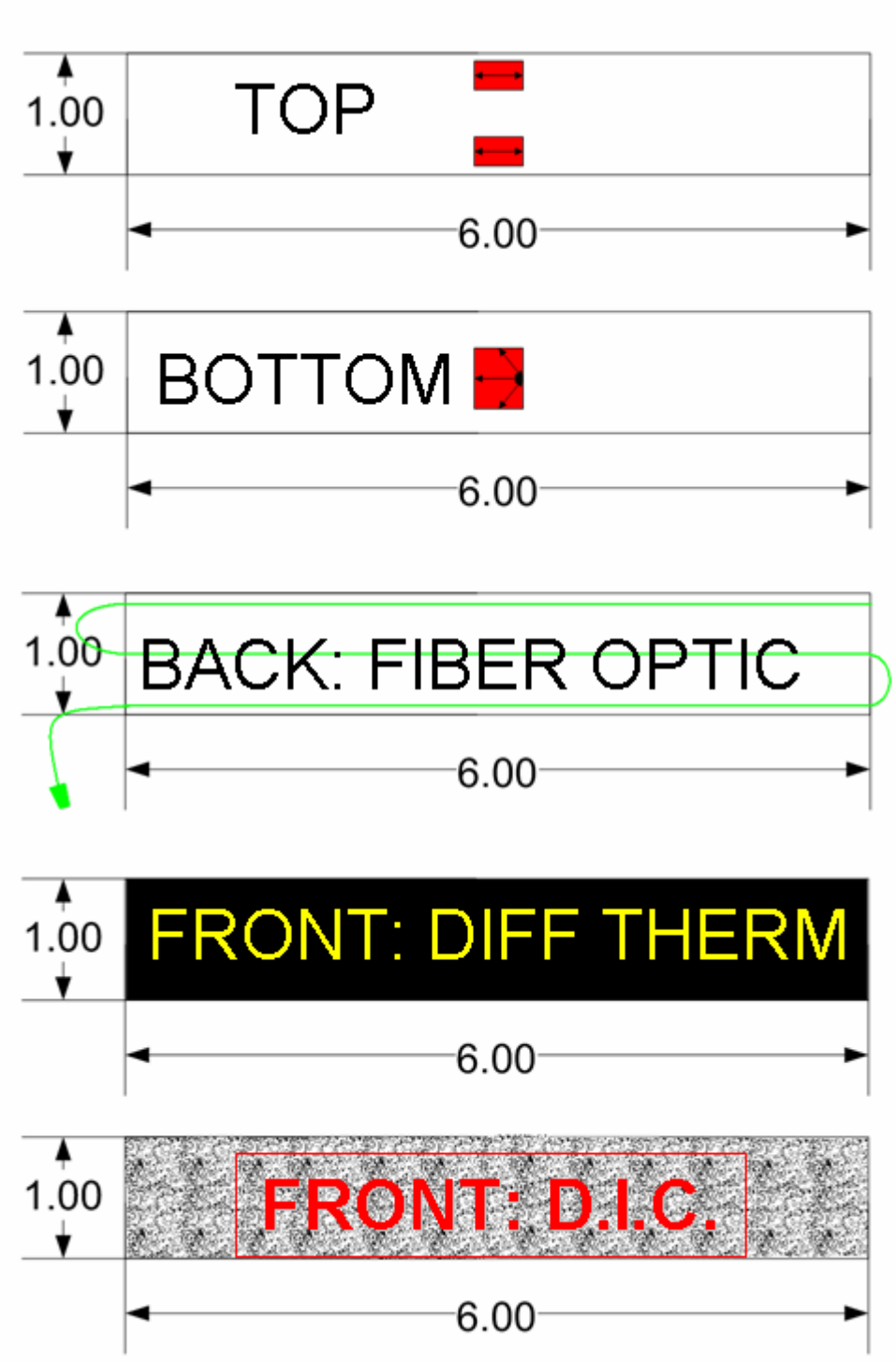

Figure 6: Specimen preparation for strain gages, fiber optic strain gages, differential infrared thermography, and digital image correlation

3.4 Testing Method

3.4.1 Test Matrix

The complete and actual test matrixes are listed in Appendix A and Appendix B, respectively. For future reference, the term ‘strong’ refers to specimens loaded with the 85% TiB / 15% Ti predominantly in compression. The term ‘weak’ refers to specimens loaded with 100% Ti predominantly in compression. Steel specimens included in the matrix were used as dummy specimens.

3.4.2 Experimental Procedure

In four-point bending, specimens were loaded under constant amplitude loading. The maximum and minimum loads were varied such that Pmax – Pmin = 1000 lbs. A ramp-up rate of 100 lbs/sec was used during testing. The test was run in load control mode using a 20 kip load card. Each specimen was subjected to loads at levels of 2.5K, (2.0-3.0K), 5K (4.5-5.5K), 10K (9.5-10.5K), 15K (14.5-15.5K), or 19.5K (19.0-20.0K), respectively. A variable amplitude load was chosen in order to accommodate the differential infrared thermography technique.

3.5 Finite Element Analysis

3.5.1 Description of Finite Element Models

The commercial finite element package ABAQUS was used to create a numerical model of the beam configuration. Seven discrete layers were chosen to represent the layered FGM structure in spite of interlayer diffusion zones present in the real structure. The manufacturer's elastic constants were used in the analysis. Linear hexahedron (C3D8) elements were used to mesh the model with the length of each symmetric element measuring 1/24". Furthermore, a quarter-model was assumed as four-fold symmetry was present in the geometry. Loads applied at each roller were assumed to be uniformly distributed over a region ¼" x 1". (¼" x ½" on the actual model)

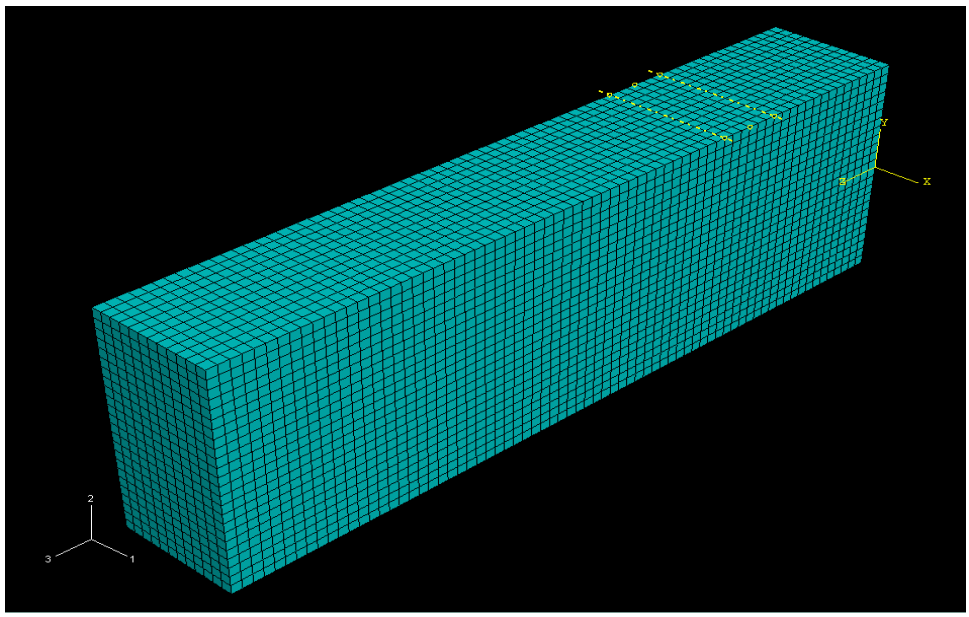

Figure 7: Meshed finite element quarter model of beam

RESULTS AND DISCUSSION

4.1 Material Deformation and Failure

Upon evaluating the failed specimens many unique observations can be concluded from the failure surfaces. When viewing the commercially pure titanium structure, it can be seen that gross plastic deformation occurred primarily in the medial region between the two upper rollers. During the testing this deformation occurred at an applied load of less than fifteen thousand pounds. Due to the nature of the loading spectrum, a more exact value was not extracted. The maximum applied load for these tests was twenty thousand pounds.

Figure 8: Deformed uniform Ti specimen after loading

For the uniform 85% TiB ceramic composite specimens, the specimens catastrophically ruptured at approximately five thousand pounds. The fracture morphology reveals that the ceramic failed from a classic brittle fracture as the fracture mirror can clearly be seen in the lower regime of the specimen. Towards the upper zone, lies a characteristic ‘lip’ prevalent in all of the uniform TiB failures.

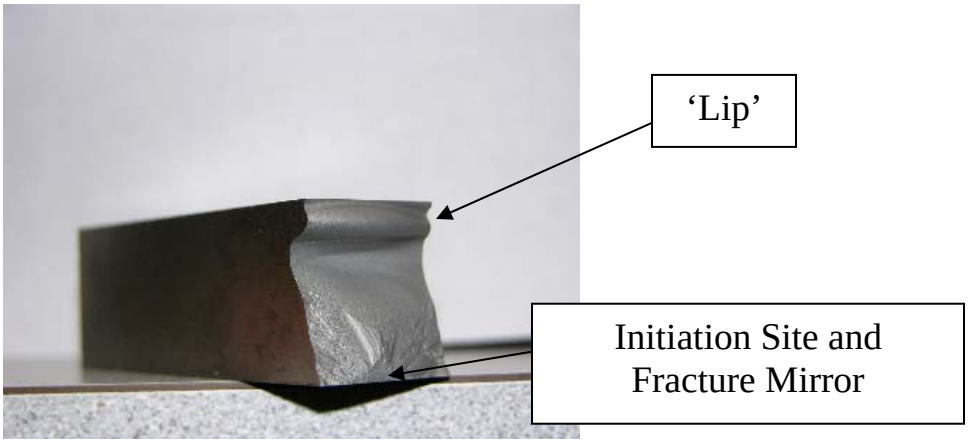

Figure 9: Failed 85% TiB / 15% Ti specimen

When the layer FGM was loaded in the weak configuration, the geometry with the ceramic in tension also ruptured catastrophically at a load level similar to that of the uniform 85% TiB. The major difference being that the characteristic 'lip' seen in the uniform ceramic composite was not present. Instead, the pure titanium layer created a 'skin' which prevented the specimen from completely breaking into two discrete parts. (The 'weak' Ti/TiB structure is pictured inverted from the loading.)

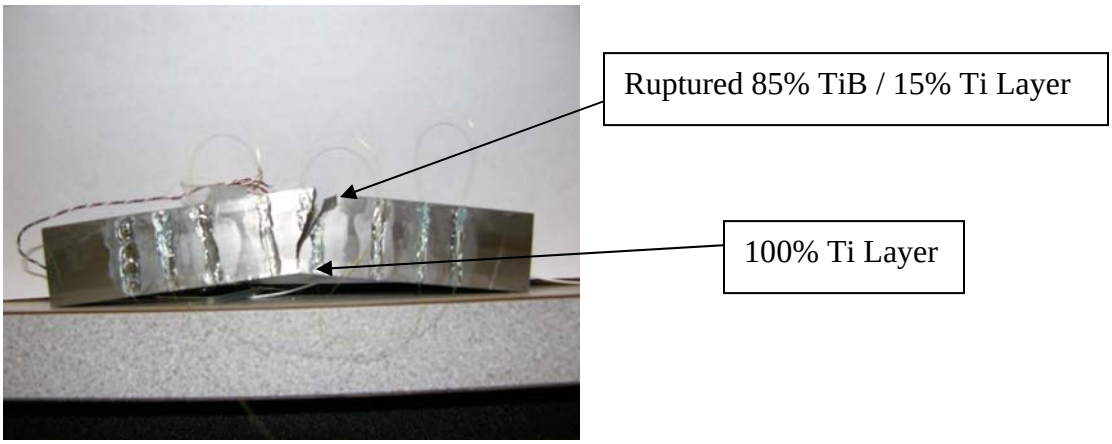

Figure 10: Failed 'weak' FGM

In a separate test in which the loading rate was increased significantly (~30 x load/sec) to completely sever the specimen, the complete fracture surface of the weak-configured FGM could be observed because the Ti layer was completely sheared. The

layering can be clearly seen internally as the surface varies from a very smooth, 85% TiB to a grainy 100% Ti layer. In the uniform titanium layer, pitting characteristic of a ductile overload was present. Furthermore, this ductile pitting does not extend beyond the region of the pure titanium allude to the fact that the failure behavior of the titanium is drastically modified when processed with the ceramic, even in small quantities. It can also be seen that the actual layer stacking sequence does not coincide with the layering specifications. This can probably be attributed to packing error and shrinkage during the sintering process.

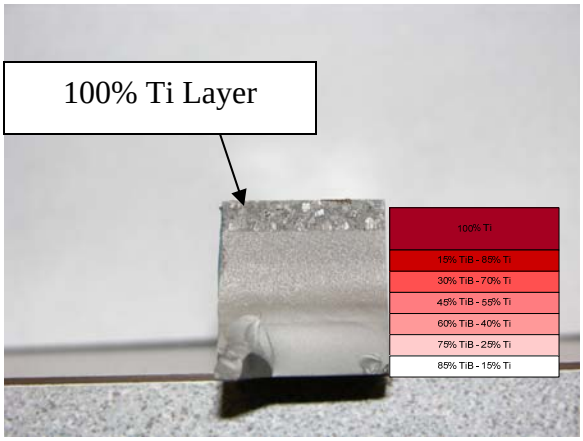

Figure 11: Fully split 'weak' FGM

Finally, when the FGM in the strong configuration was loaded up to twenty-thousand pounds, no signs of rupture or gross plastic deformation could be detected. [Figure 12] This behavior proves that the 'strong' FGM configuration is in fact stronger than the 'weak' configuration. Therefore, when strictly comparing failure strength for design, the strong-configured FGM is an improvement over both uniform titanium and 85% TiB in this configuration.

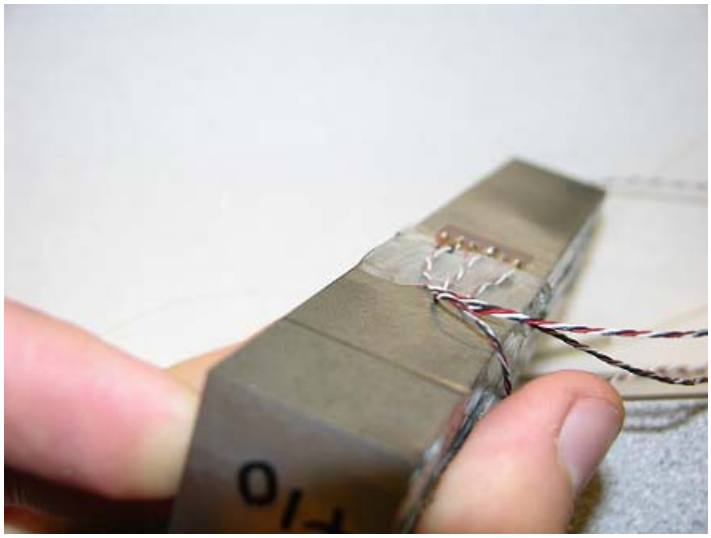

Figure 12: ‘Strong’ functionally graded beam after testing

4.2 Strain Gage Results

Although strain gages were laid on most of the specimens during testing, only limited data was acquired. [Figure 13] Although the four-point bend test allowed for strain gages to be placed on the upper surface of the specimen, small amounts of room on the upper surface in which the wire had to be redirected caused the wiring to oftentimes prematurely delaminate. Furthermore, the weak configuration specimens and uniform 85% TiB / 15% Ti specimens were susceptible to rapid failure and at the desired 10K loading level.

On two 'strong' specimens, F05 and F10, data was acquired with reasonable accuracy. From the results, it can be seen that the specimen follows a linear trend up until thirteen hundred μstrain at which the gage delaminated. Additionally, the data for the compressive zone demonstrates a higher degree of scatter than its tensile counterpart. It is speculated that this was caused by the gage measuring compression being disrupted by the upper roller's close proximity.

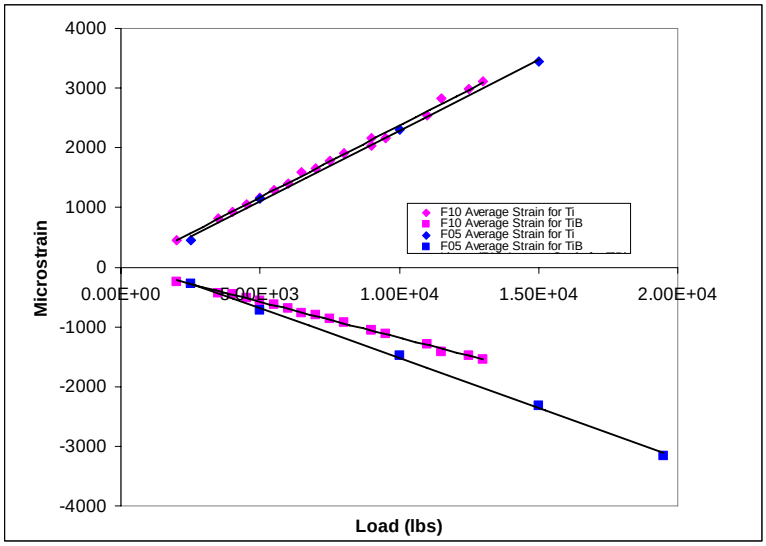

Figure 13: Strain gauge data for specimens F05 and F10

4.3 Digital Image Correlation Results

As the strong configuration would be the preferential geometry to use in a real application, the strain field for the strong FGM was analyzed for ε_{xx} on the undeformed shape by comparing the finite element analysis to the digital image correlation. Strain field data was only gathered for the regions in between the two lower rollers in order to give the camera a better focus on the speckle pattern.

In Appendix C, digital image correlation results were plotted at three arbitrary times during the course of the test run in order to improve the statistical significance. Contours were plotted using fourteen color increments with varied upper and lower bound values at +/- 3000, 2000, 1000, 500, and 0. Zero runs are nominally zero as contour values were actually set to +/- 1e-10. Field values which exceed the upper bound were colored red. Likewise, negative field values which go below the lower bound were colored purple. The color green represents values which are closest to zero in the color contour.

Upon observing the images, a disjuncture between the strain data and the digital image can be observed at the boundaries. This is a byproduct of the digital image correlation routine and not of the cropping used to select the area of interest.

When viewing the results, the upper region correctly displays a compressive zone and the lower region correctly displays a tensile zone in accordance with the basic bending theory. Also apparent is that the compressive zone is much smaller than the tensile zone in the ‘strong’ FGM.

As the contour is decreased to zero, this is verified by the neutral axis shifting from an ideally neutral position to one closer to the compressive surface. [Figure 14] An

averaged line can be used to estimate the position of the neutral axis at a region approximately 3/8” from the top surface. However, in reality, the ‘neutral axis’ is really a ‘neutral boundary’.

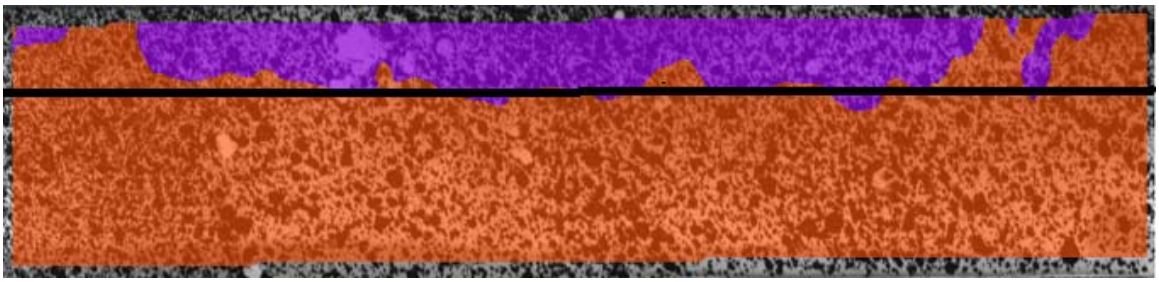

Figure 14: Estimated neutral axis for Ti/TiB FGM

4.4 Differential Infrared Thermography Results

Upon comparing the differential infrared thermography results for the pure titanium, ‘strong’ FGM, and 85% TiB / 15% Ti, the characteristic compressive and tensile zones can be seen on the top and bottom surfaces of each image. Furthermore, the highly compressive zones surrounding the fixture’s rollers are also made obvious. In the titanium image, a blemish caused by a coating anomaly can also be observed. [Figure 15]

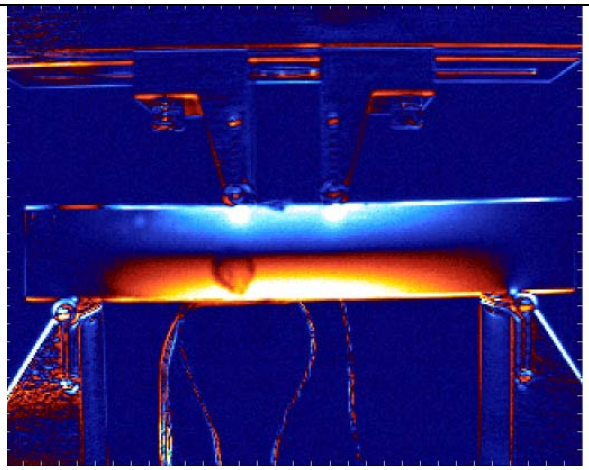

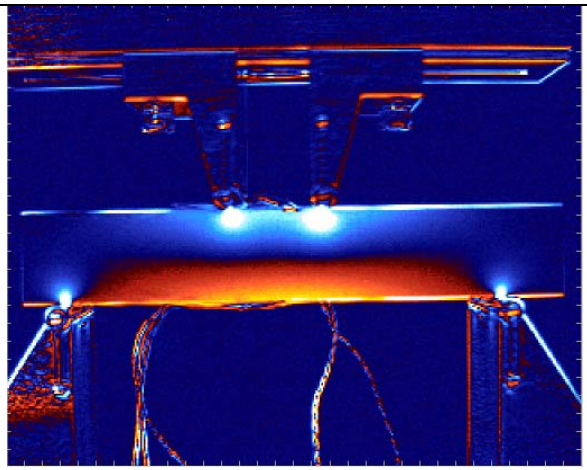

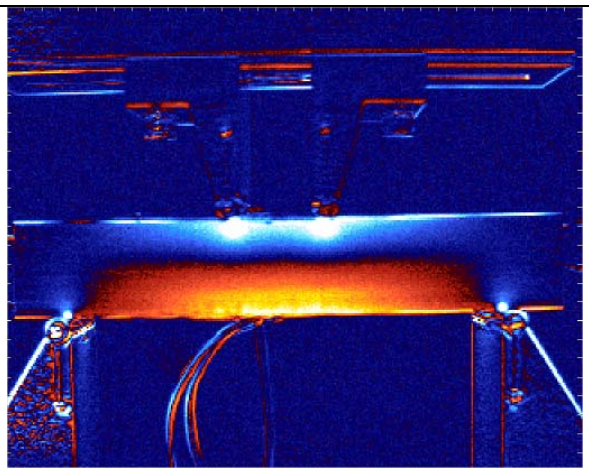

Figure 15 – Differential infrared thermography digital image results for Ti, Ti/TiB FGM, and 85% TiB / 15% TiB at 2.5K

Upon extracting the pixilated quantities of stress from the ‘half-line’, a line parallel to the loading axis through the front surface of the middle of the specimen, it can be seen that the ‘strong’ FGM results do not lay at an intermediate position between the uniform titanium and the uniform 85% TiB / 15% Ti. [Figure 16] Instead, a bowing is present. This occurs because of the unequal sharing of stress caused by the modulus mismatch and the layer stacking sequence.

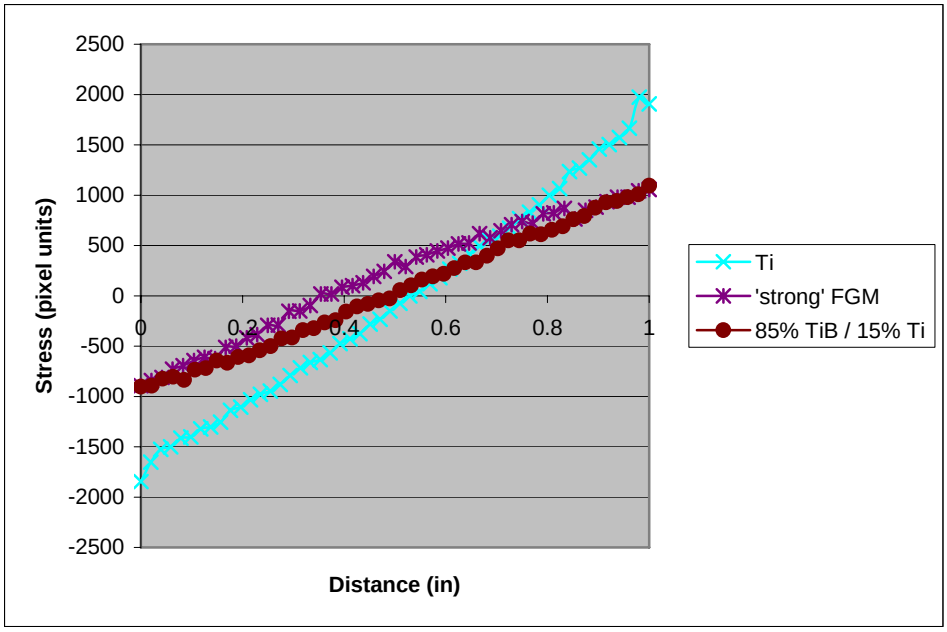

Figure 16: Comparison of stresses from differential thermography at 2.5K for Ti, 'strong' FGM, and 85% TiB / 15% Ti

Thermography results could not be directly overlaid to finite element stress results because the stepped gradation prevented the calculation of stress to pixilation ratio. A strain gage would have had to span overtop multiple layers. Although this could have been used to create a rough approximation of the conversion between pixels and stress, the accuracy of the differential thermography system would be blemished by the weak conversion. Another usage would have been if a strain gage small enough to fit overtop each layer could have been found, each layer could have been accurately converted. Therefore, the results were normalized based upon the maximum stress in each material set in order to form a comparison. [Figure 17]

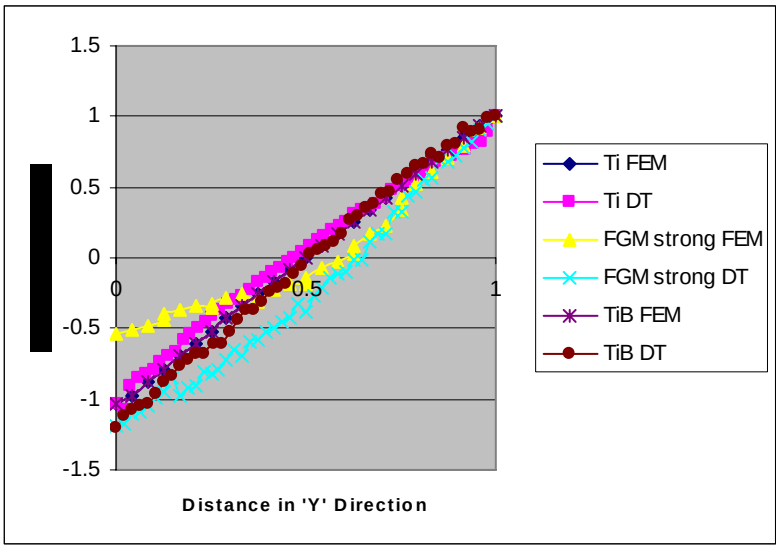

Figure 17: Comparison of normalized stresses for FEM and differential infrared thermography at 2.5K for Ti, 'strong' FGM, and 85% TiB / 15% Ti

When normalizing, the uniform Ti and 85% TiB exhibit the exact same behavior, a linear relationship, because the internal stresses are identical for a homogenous material in the linear regime. The experimental results show similar agreement except with some deviation: the Ti was slightly above and the 85% TiB was slightly below the FEM results. On the other hand, the functionally graded materials showed significant deviation, particularly around the compressive zone within the regime of the ceramic composite. This may be caused in part by the gross material property scatter of the Ti/TiB composite. Appendix D shows the variation in elastic modulus scatter from two separate sources.

Because of the lack of conversion factor, a stress magnitude was determined from the finite element results along the same plane. [Figure 18] From these results, the predicted stresses for the homogenous materials are between +/-12 ksi and +8 to -15 ksi for the 'strong' FGM when loaded at 2.5K. It can also be observed the neutral axis for the FGM will be shifted to increase the total size of the tensile zone as predicted from

experimental digital image correlation results. In essence, the stiffer structures are taking away more stress from the less rigid layers.

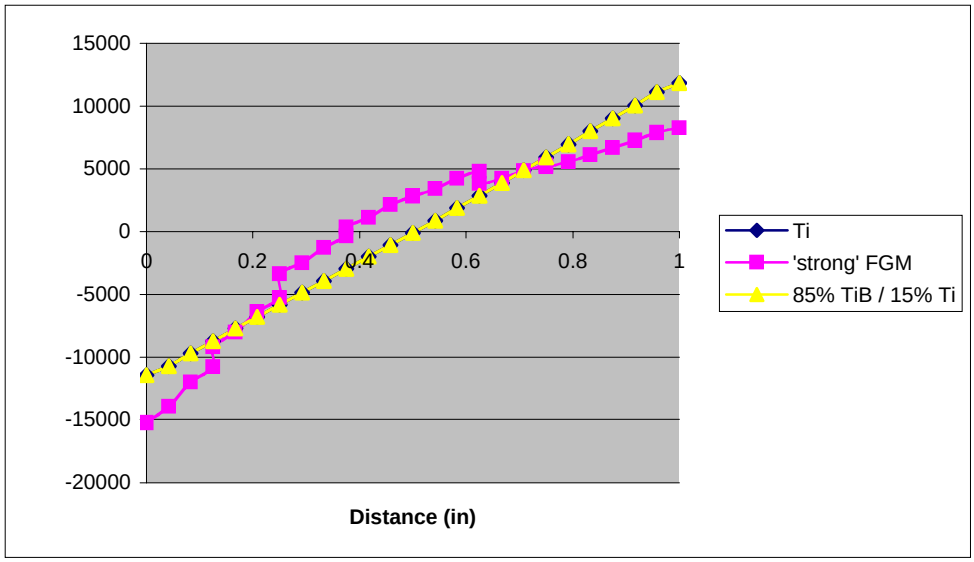

Figure 18: Comparison of stresses ($\sigma_{xx} + \sigma_{yy}$) for FEM and differential infrared thermography at 2.5K for Ti, 'strong' FGM, and 85% TiB / 15% Ti

4.5 Fiber Optic Strain Gage Results

Limited amounts of data were acquired using the fiber optic strain gages because the propensity of the fibers to break during handling. These fibers are better suited for usage in plates and panels where disruptive bending would be unlikely to occur once the fiber had been laid. Also, the number of passes able to be performed by a single fiber was limited by the ability of the fiber to 'loop'. Based upon the length of the one meter fiber, six passes were to be performed. This proved difficult because of the tight radius of the loop incurred having the fibers closely together.

Originally, some of the fiber optic gages were placed parallel to the loading axis. Unfortunately, because the fiber sensors only determined an average reading every six millimeters at the location of each sensor, the configuration was useless and didn't provide meaningful readings to quantify the interlayer effects. Additionally, the strains and stresses in the 'y' direction were so low around the mid-plane parallel to the loading direction that meaningful strain data would have been more easily acquired when dealing with higher stresses. In order to achieve more meaning results to study interfacial zones, smaller Bragg Grating regions would have to be created.

4.6 Comparison of FEA and Digital Image Correlation Results

When overlaying the finite element analysis results to the digital image correlation, a great amount of correlation can be determined. Although the tensile regions show some disconnect at higher strain contour values, this can in part be attributed to overlay error between the two techniques. Appendix E summarizes the overlay of digital image correlation and finite element analysis results. Probably the most convincing evidence of the finite element analysis successfully predicting the elastic behavior of the functionally graded Ti/TiB is the excellent determination of the shape of the compressive zone. [Figure 19] Not only did the magnitudes appear to very accurately align but also a 'double hump' was accurately mirrored.

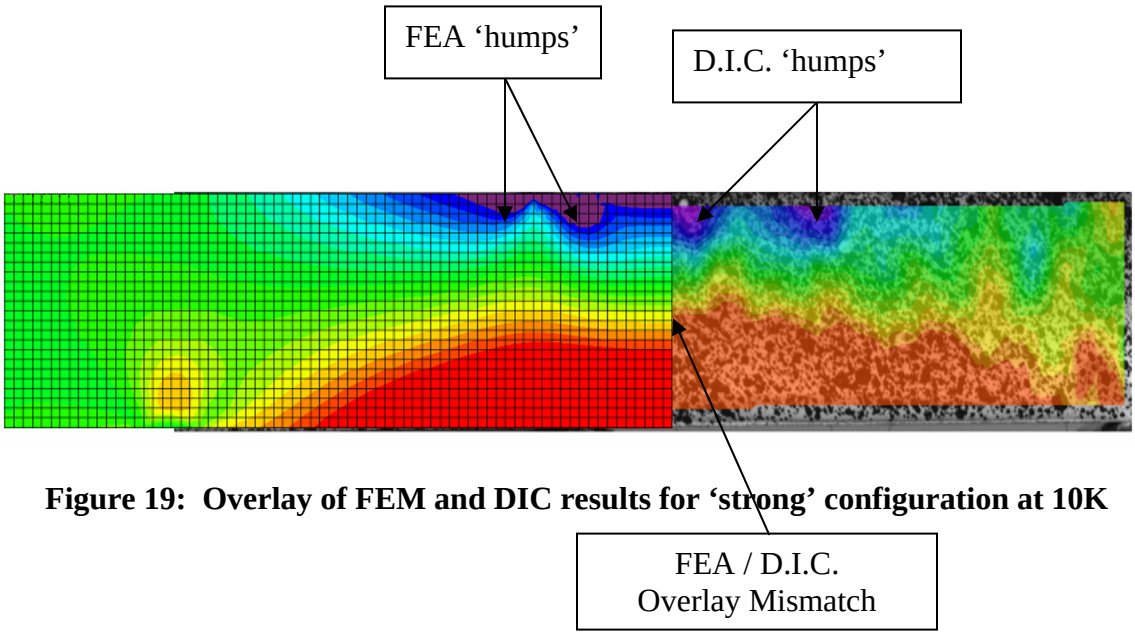

Figure 19: Overlay of FEM and DIC results for 'strong' configuration at 10K

4.7 Overlay of Several Measurement Techniques

The strain field results along a horizontal line 1/8” from the bottom surface were compared for the digital image correlation, fiber optic strain gages, and finite element analysis results. [Figures 20, 21] Strain gage data was also overlaid as an upper bound. Multiple images and multiple line splices were used to gather data for the digital image correlation in order to help reduce error caused by camera misalignment. Data from the fiber optic strain gage and strain gage were determined from specimen F05.

Figure 20: Slice of profile of specimen used to gather overlaid data

From these results, it can be seen that the digital image correlation most closely relates to the finite element analysis results. The error in the fiber optic strain gaging can be attributed to the tendency of the fiber to bow on the specimen during application. Furthermore, because sensors locations were not accurately determined, the data could be shifted on the ‘x’ axis in order to further collapse the results.

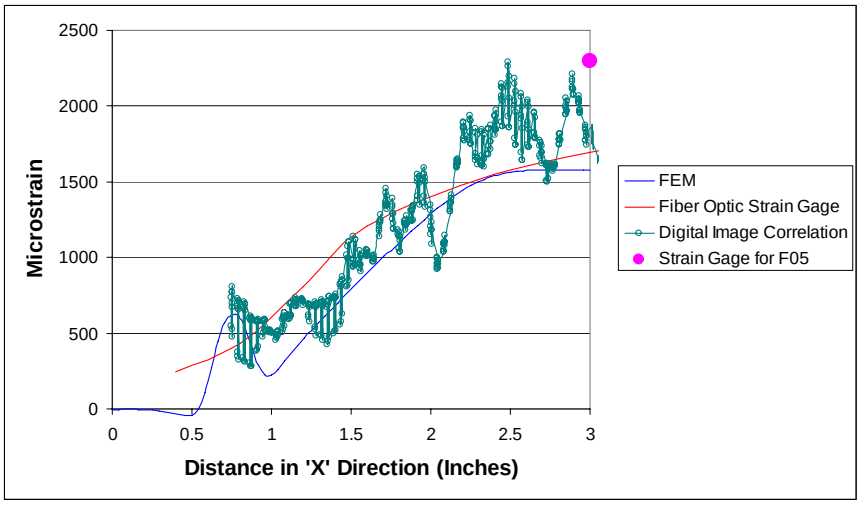

Figure 21: Overlay of Several Measurement Techniques

Certain assumptions can be made in order to better collapse this data onto the finite element analysis results. First, since the actual sensor location for each fiber was not accurately found at least four millimeters of shifting in the 'x' direction could occur. Next, because of errors caused by the electronic process of extracting linear data from a digital image in digital image correlation, the theoretical results for the finite element analysis can be shifted 1/24" to match this error. In this case, FEA was modified instead of the digital image correlation because the results could be moved to a precise location. Furthermore, since the fiber optic Bragg fibers had some degree of movement caused by a 'bowing' effect when laid, this assumption also holds true in conjunction with the fiber gage results. When viewing the corrected overlay, a move convincing fit of the data is now more plausible. [Figure 22]

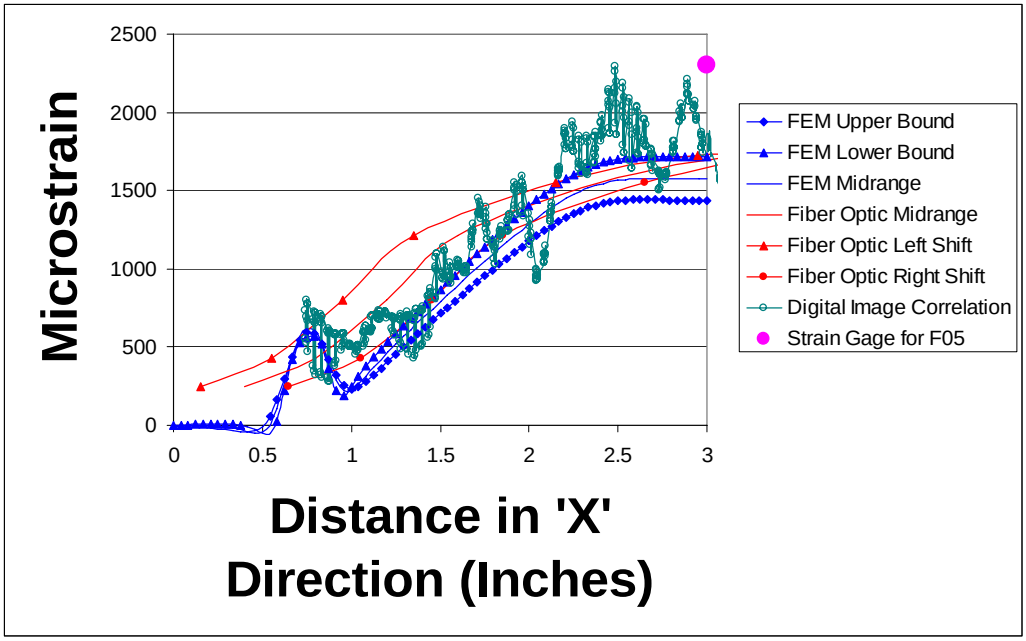

Figure 22: Corrected overlay data

4.8 Stress Field Comparison of Strong and Weak Configurations

When comparing the stress fields of the 'strong' and 'weak' configurations, many differing characteristics became apparent. In the σ_{xx} field for the 'strong' configuration, the compressive stresses in the upper, compressive zone have higher absolute stresses than the lower, tensile zone. On the contrary, for the weaker configuration, the lower tensile region experiences higher absolute stresses. It can be concluded that the stiffer layers are withstanding higher amounts stress. [Appendix F]

In the σ_{yy} field, two large compressive zones show the locations of the stresses created by the rollers. Less obvious is the tensile region coupled to the upper roller. For the 'strong' configuration, this stress is much higher and broader than the tensile region in its 'weak' counterpart.

The 2D shear stress field, σ_{xy} , has four distinctive regions of interest: the lower roller, the upper roller, the mid-zone, and the tensile coupling to the upper roller. In the 'strong' configuration, the higher shear stresses again gravitate towards the stiffer tensile region. This could have been predicted by the behavior of the prior two examined fields.

Finally, the Von Mises shows the combined effects from the σ_{xx}, σ_{yy}, and σ_{zz}. As was concluded from the σ_{xx}, the higher stresses are found in the region of the stiffest material, the 85% Ti/TiB.

When comparing these results to the failure behavior, it becomes more obvious as to the definitive reason as to why the FGM was stronger than both the uniform Ti and uniform 85% TiB / 15% Ti. Not only did the FGM take advantage of placing the ceramic in compression to negate the obvious weakness of ceramic tensile rupture, but it also

diverted some of the strain energy away from the weaker titanium layer. This assumes that the titanium is undesirable after yield. Therefore, when optimizing a functionally graded structure, it is very important to recognize this tradeoff in order to maximize the strength.

CONCLUSIONS AND RECOMMENDATIONS

5.1 Conclusions

During this testing, the digital image correlation was found to be the better choice than differential thermography for acquiring accurate field measurement for several reasons. First, the values acquired by the digital image correlation system were independent of the material system in usage. This means that any layering configuration of the Ti/TiB functionally graded material could have been used to acquire meaningful data. Not only does the differential thermography system require some form of strain gage on each layer to measure stress, but it also dictated that the load spectrum had to be varied at a high enough frequency to acquire photons emitted due to the thermoelastic effect. The D.I.C. camera was also less sensitive to environmental easier to set up as it did not require cooling nor calibration for 2D imagery. Furthermore, because definitive magnitudes of strain were achieved, the results could be compared with finite element results quite effectively. Differential thermography would have been much more successful if a calibration value could have been determined. This would have resulted in actual stress magnitudes rather than normalized results.

In the laboratory, the fiber optic strain gages offered very little benefit over the digital image correlation because it measured only a fragment of the total amount the same field data. Furthermore, the fiber gages provided an averaging of the strain about the fiber sensor length; this was not very beneficial for attempting to measure the region across each of the material boundaries. However, the real benefit of the fiber optic system is that it does not require a stationary camera system. In scenarios where space,

lighting, and a level surface are not available, the fiber optic gages may be the ideal choice to use to measure a linear region of the strain field.

Finally, conventional strain gages worked reasonable well under the laboratory air and room temperature conditions. However, if specimens were subjected to varying or higher temperature conditions, calibrating the gages and selecting the proper gages would become significantly because the gages would have to be temperature compensated. Not only would interlayer zones be very difficult to calibrate but batch material variation amongst the uniform layered ceramic composites would also be of concern. Furthermore, when selecting a strain gage, a different gage would have to be chosen for each layer for optimal results.

Another conclusion is that the finite element modeling accurately predicted the elastic behavior of a functionally graded titanium/titanium boride beam under small displacements. Although this was not the main purpose of this work, the overlay of the finite element results strain field to the digital image correlation showed excellent correlation between laboratory testing and numerical results. Furthermore, a novel approach to finding the location of the neutral axis or neutral 'boundary' was also determined.

Also of some interest, the reported surfaces of the functionally graded Ti/TiB and uniform 85% TiB / 15% Ti were observed. It was seen that the rupture face of the composite lacked the same brittle rupture characteristics of the 85% TiB / 15% Ti. When comparing the permanent deformation of the FGM in the 'weak' and 'strong configurations, uniform Ti, and uniform 85% TiB / 15% Ti when loaded up to 20K lbs, it

was found that the functionally graded material in the ‘strong’ configuration was the best design configuration.

5.2 Recommendations

An advantage of digital image correlation is that it has the potential to view images at the smaller level based upon the resolution of a microscope rather than a conventional camera. Zang and others have already investigated the use of this type of system to measure the elastic modulus in this fashion. [Zang, 2005] Smaller scale analysis for functionally graded materials would be particularly valuable in that interfaces between layers or layering gradients could more accurately measured. At the current scale run during these experiments, a pixel would span approximately 1/100". If zoomed in ten to one hundred times, the change in strain about that region could be more readily deciphered. This information could be used to gauge the quality of the layer bonding and the material system.

Fiber optic gages proved to be very likely to break for this form of testing. When designing specimens, a larger, flatter work surface would be more ideal for usage of the fiber gages. Also tools for more accurately laying the gages would have helped to reduce fiber 'bowing'.

Before the work began, it was believed that the material properties had tighter bounds. Better knowledge of the elastic properties of the Ti/TiB layers could have possibly improved the analysis of the functionally graded system in conjunction with the laboratory results.

Appendix A –Specimen Configuration Matrix

Specimen ID	Material	Front Top	Back Bottom	Fiber Direction	Top Face
s01	Low-Carbon Steel	D.I.C. Gage	Gage		
s02	Low-Carbon Steel	D.I.C. Gage	Gage		
s03	Low-Carbon Steel	D.I.C. Gage	Gage		
s04	Low-Carbon Steel	D. T. Gage	Gage		
s05	Low-Carbon Steel	D. T. Gage	Gage		
s06	Low-Carbon Steel	D. T. Gage	Gage		
t01	Comercially Pure Titanium	D.I.C. Gage	Fibers Gage	H	
t02	Comercially Pure Titanium	D.I.C. Gage	Fibers Gage	H	
t03	Comercially Pure Titanium	D.I.C. Gage	Fibers Gage	V	
t04	Comercially Pure Titanium	D. T. Gage	Gage		
t05	Comercially Pure Titanium	D. T. Gage	Gage		
t06	Comercially Pure Titanium	D. T. Gage	Gage		
b01	85% TiB / 15% C.P. Ti	D.I.C. Gage	Fibers Gage	H	
b02	85% TiB / 15% C.P. Ti	D.I.C. Gage	Fibers Gage	H	
b03	85% TiB / 15% C.P. Ti	D.I.C. Gage	Fibers Gage	V	
b04	85% TiB / 15% C.P. Ti	D. T. Gage	Gage		
b05	85% TiB / 15% C.P. Ti	D. T. Gage	Gage		
b06	85% TiB / 15% C.P. Ti	D. T. Gage	Gage		
f01	Ti/TiB FGM	D.I.C. Gage	Fibers Gage	H	cp Ti
f02	Ti/TiB FGM	D.I.C. Gage	Fibers Gage	H	cp Ti
f03	Ti/TiB FGM	D.I.C. Gage	Fibers Gage	H	cp Ti
f04	Ti/TiB FGM	D.I.C. Gage	Fibers Gage	V	TiB
f05	Ti/TiB FGM	D.I.C. Gage	Fibers Gage	V	TiB
f06	Ti/TiB FGM	D.I.C. Gage	Fibers Gage	V	TiB

f07	Ti/TiB FGM	D. T. Gage Fibers Gage	V	cp Ti
f08	Ti/TiB FGM	D. T. Gage Fibers Gage	V	cp Ti
f09	Ti/TiB FGM	D. T. Gage Fibers Gage	V	cp Ti
f10	Ti/TiB FGM	D. T. Gage Fibers Gage	H	TiB
f11	Ti/TiB FGM	D. T. Gage Fibers Gage	H	TiB
f12	Ti/TiB FGM	D. T. Gage Fibers Gage	H	TiB

Appendix B –Test Matrix

Specimen ID	Material	Front	Config.	Tested	S.G.	D.I.C.	D.T.	Fiber
t01	Comercially Pure Titanium	D.I.C.						
t02	Comercially Pure Titanium	D.I.C.		X		X*		
t03	Comercially Pure Titanium	D.I.C.						
t04	Comercially Pure Titanium	D. T.						
t05	Comercially Pure Titanium	D. T.		X			X*	
t06	Comercially Pure Titanium	D. T.						
b01	85% TiB / 15% C.P. Ti	D.I.C.						
b02	85% TiB / 15% C.P. Ti	D.I.C.		X		X*		
b03	85% TiB / 15% C.P. Ti	D.I.C.						
b04	85% TiB / 15% C.P. Ti	D. T.						
b05	85% TiB / 15% C.P. Ti	D. T.		X		X*		X
b06	85% TiB / 15% C.P. Ti	D. T.						
f01	Ti/TiB FGM	D.I.C.	weak	X			X*	X
f02	Ti/TiB FGM	D.I.C.	weak					
f03	Ti/TiB FGM	D.I.C.	weak					
f04	Ti/TiB FGM	D.I.C.	strong	X	X*			
f05	Ti/TiB FGM	D.I.C.	strong	X	X			
f06	Ti/TiB FGM	D.I.C.	strong	X				
f07	Ti/TiB FGM	D. T.	weak	X			X*	
f08	Ti/TiB FGM	D. T.	weak	X				
f09	Ti/TiB FGM	D. T.	weak	X				
f10	Ti/TiB FGM	D. T.	strong	X	X		X*	X
f11	Ti/TiB FGM	D. T.	strong					
f12	Ti/TiB FGM	D. T.	strong					

X* Data was tested but did not yield presentable results

Appendix D – Digital image correlation results for 'strong' FGM at different contour limits

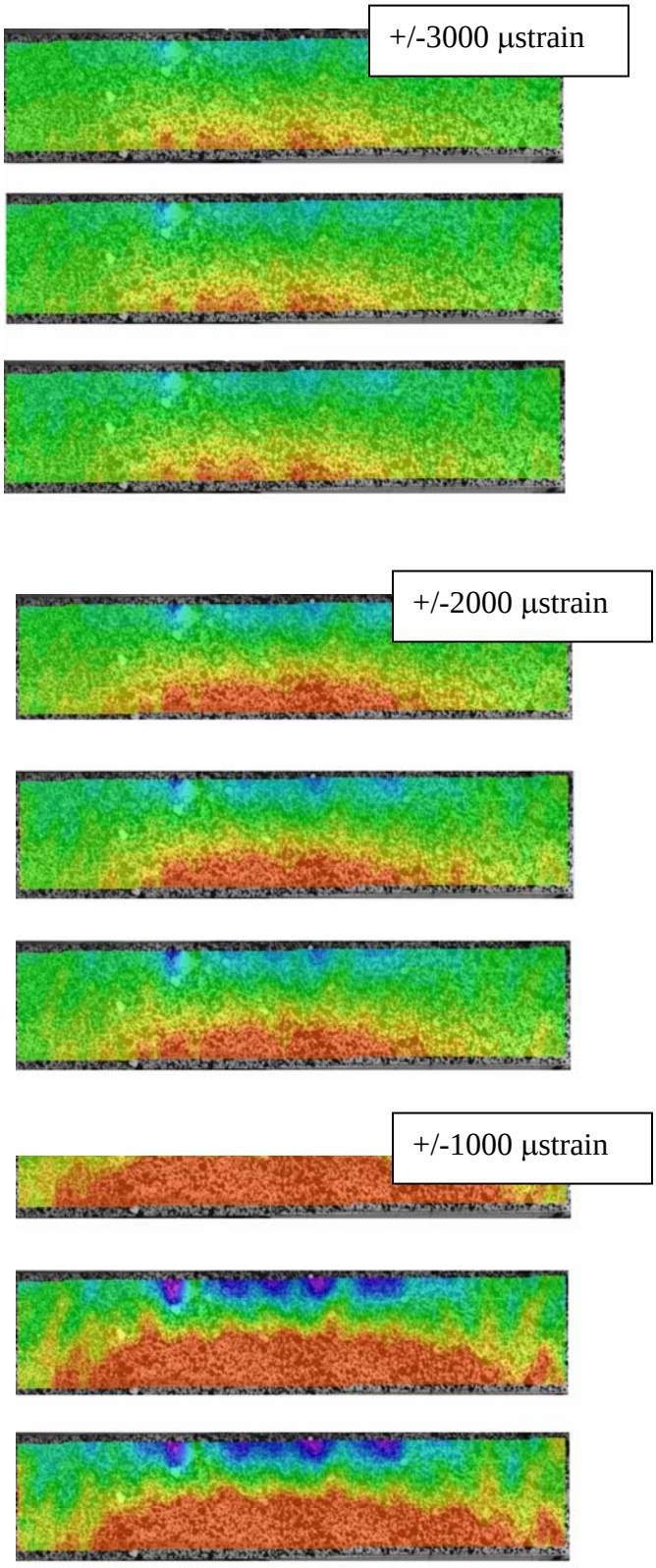

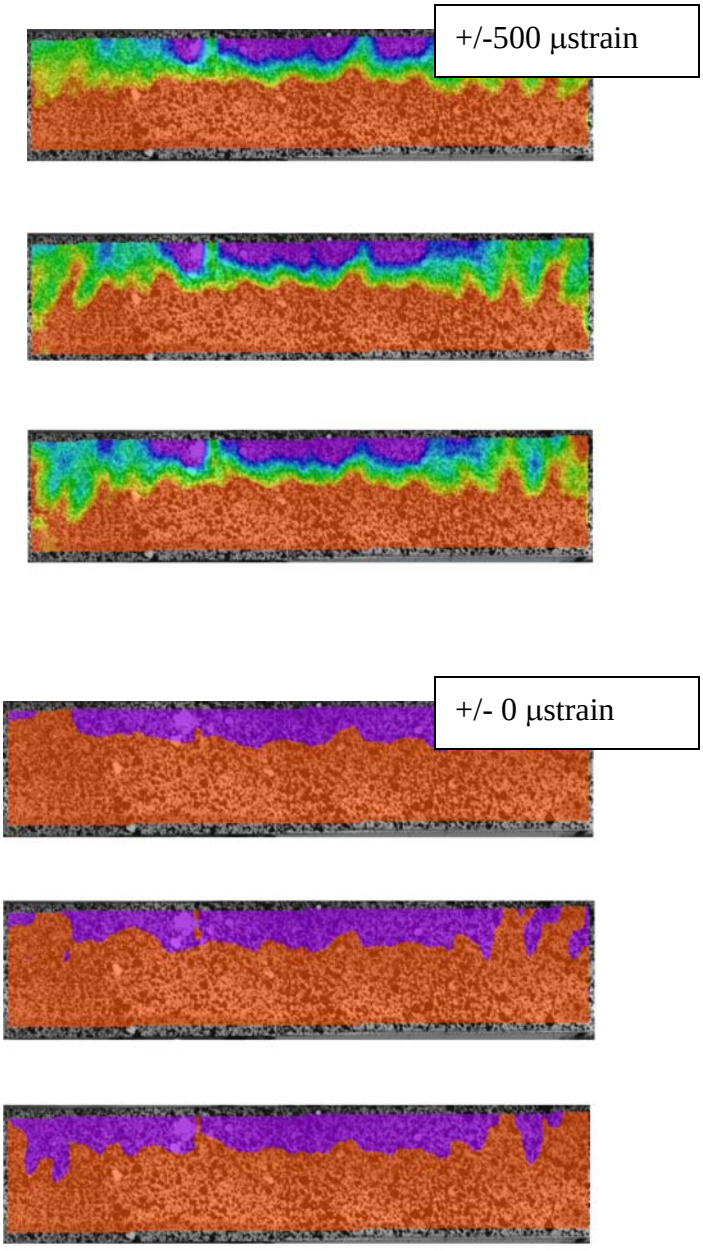
+/-500 μstrain
+/- 0 μstrain

Appendix D – Comparison of Ti/TiB Elastic Material Property Values

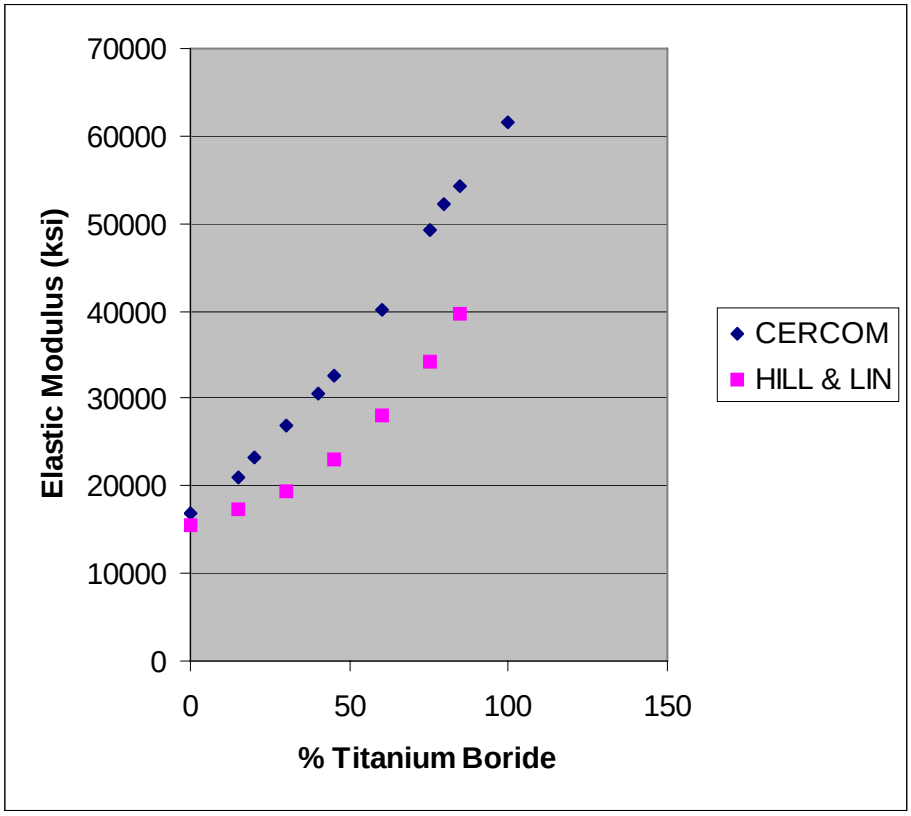

Appendix E – Digital Image Correlation / Finite Element Analysis Overlays

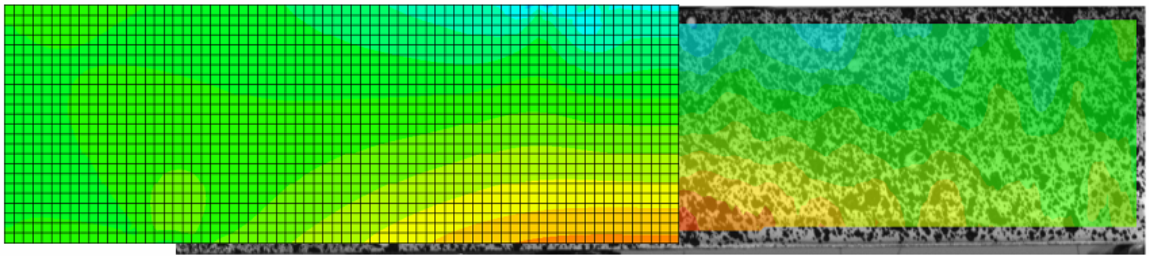

+/- 3000 μstrain

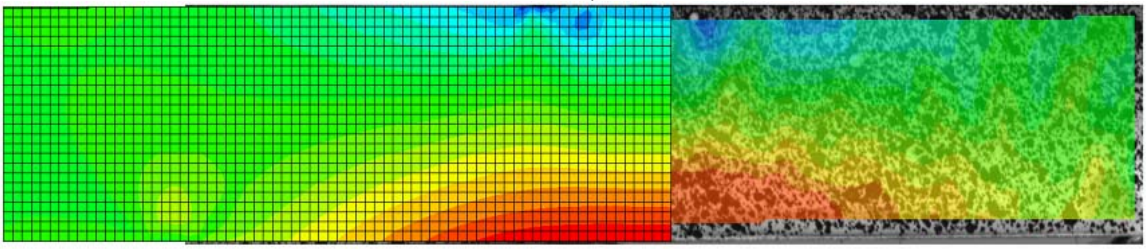

+/- 2000 μstrain

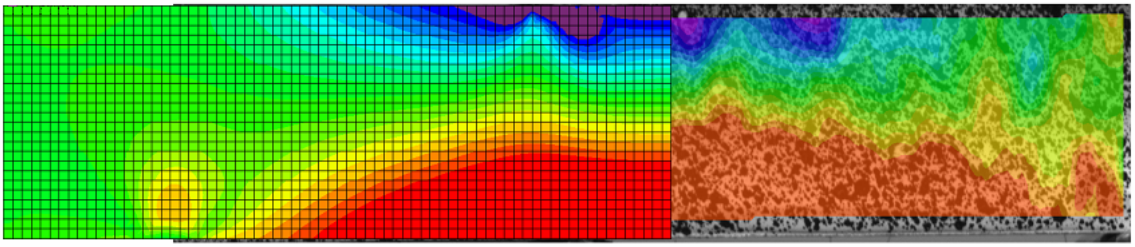

+/- 1000 μstrain

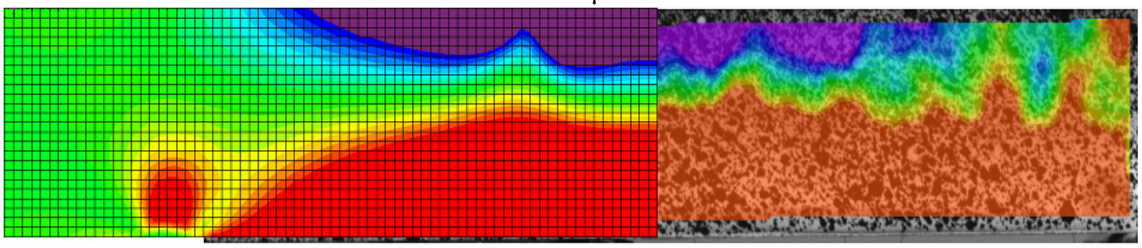

+/- 500 μstrain

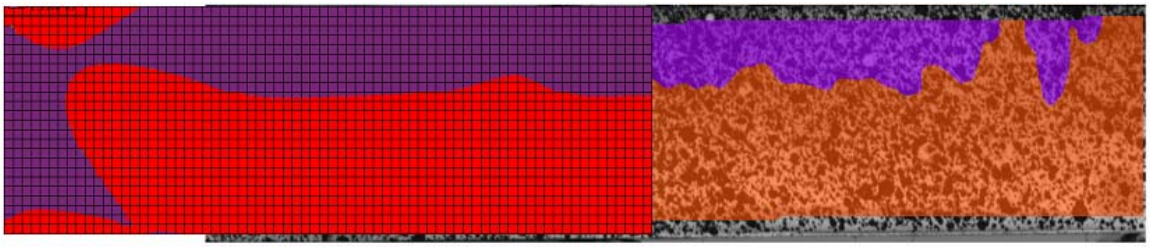

+/- 0 μstrain

Appendix F – ‘Strong’ and ‘Weak’ FGM Stress Fields at 10K with FEM

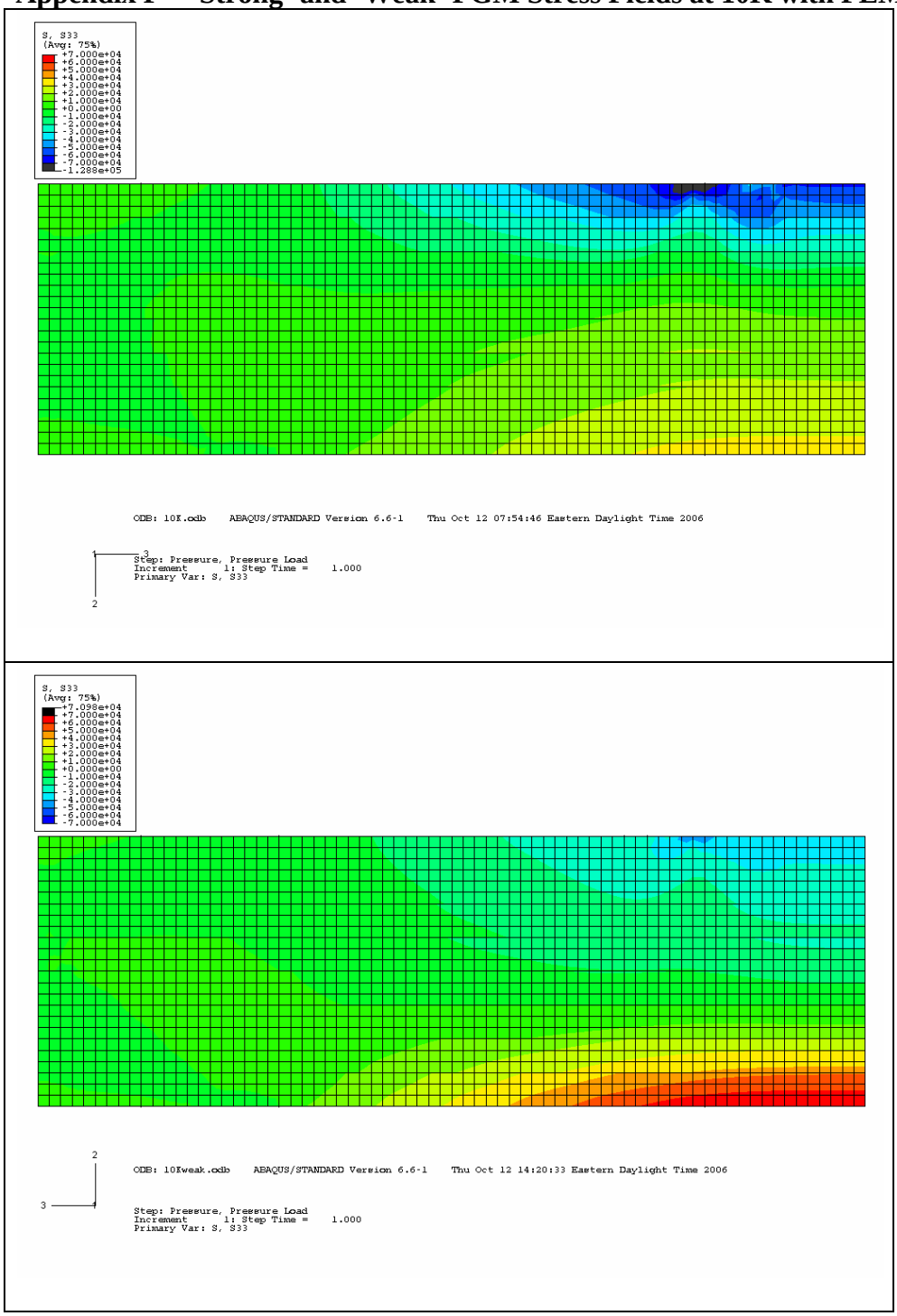

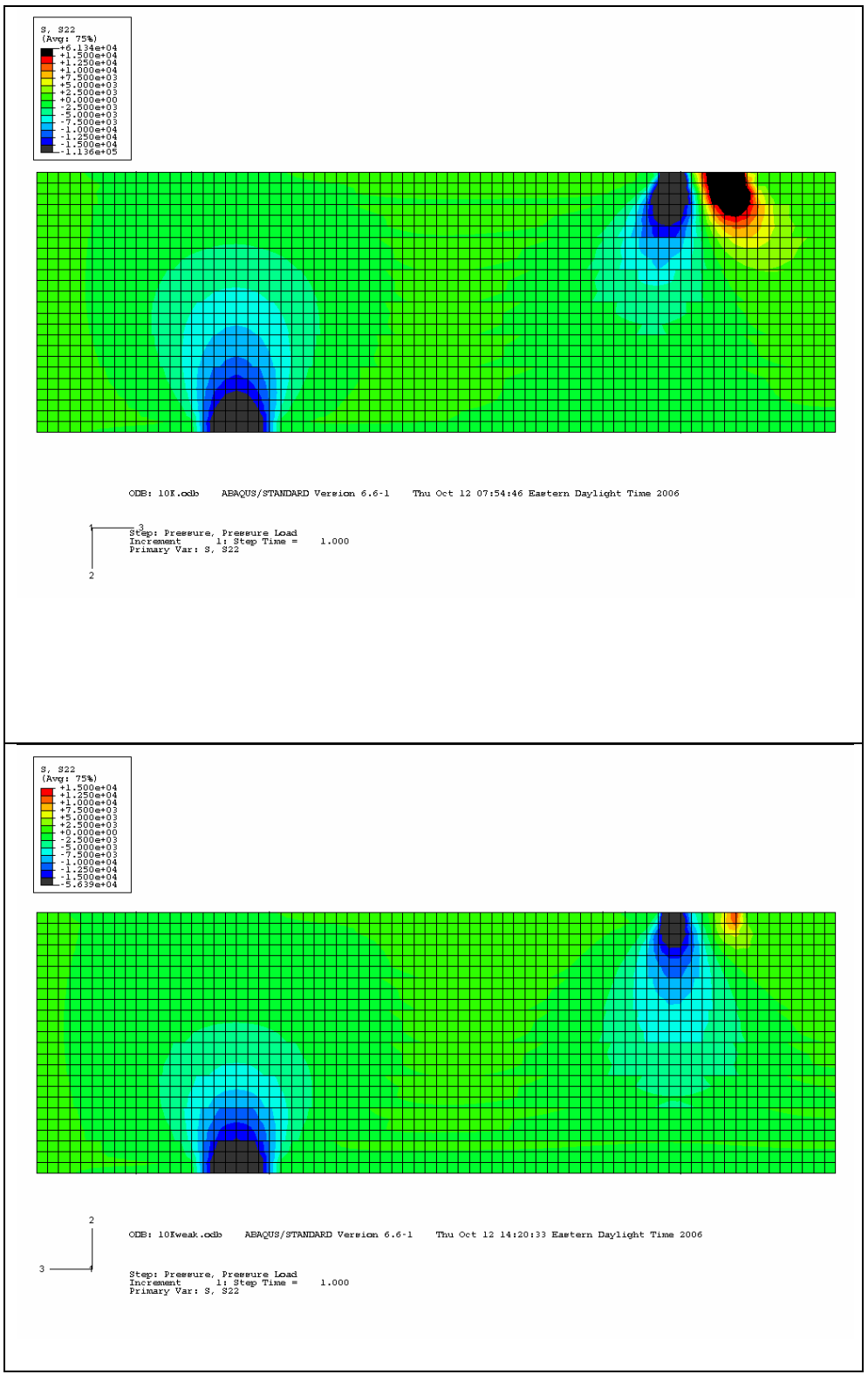
S, S22
(Avg: 75%)
+6.134e+04
+1.500e+04
+1.250e+04
+1.000e+04
+7.500e+03
+5.000e+03
+2.500e+03
+0.000e+00
-2.500e+03
-5.000e+03
-7.500e+03
-1.000e+04
-1.250e+04
-1.500e+04
-1.136e+05
ODB: 10I.odb ABAQUS/STANDARD Version 6.6-1 Thu Oct 12 07:54:46 Eastern Daylight Time 2006
3
1
2
Step: Pressure, Pressure Load
Increment 1: Step Time = 1.000
Primary Var: S, S22
S, S22
(Avg: 75%)
+1.500e+04
+1.250e+04
+1.000e+04
+7.500e+03
+5.000e+03
+2.500e+03
+0.000e+00
-2.500e+03
-5.000e+03
-7.500e+03
-1.000e+04
-1.250e+04
-1.500e+04
-5.639e+04
2
3
ODB: 10Iweak.odb ABAQUS/STANDARD Version 6.6-1 Thu Oct 12 14:20:33 Eastern Daylight Time 2006
Step: Pressure, Pressure Load
Increment 1: Step Time = 1.000
Primary Var: S, S22

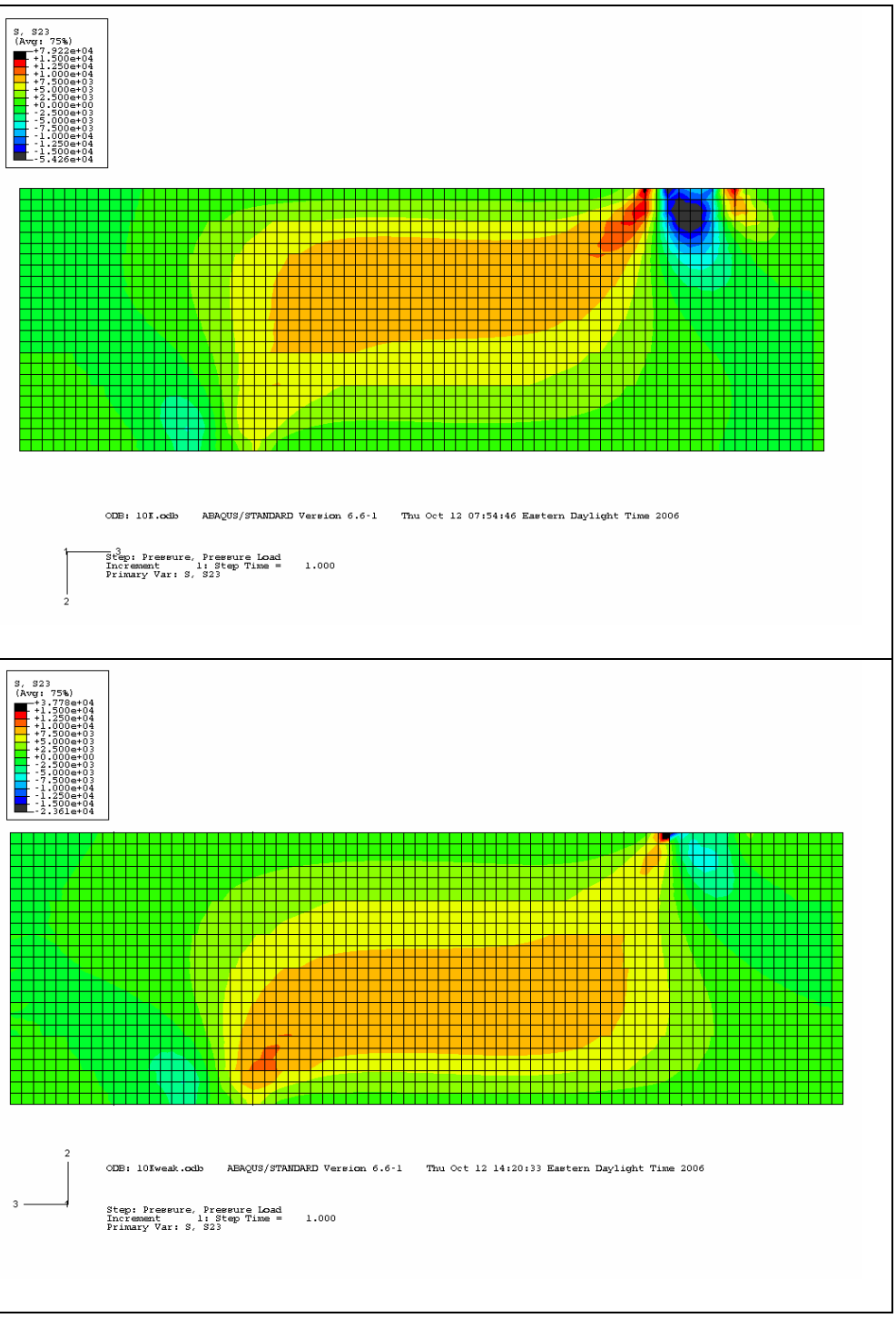
S, S23
(Avg: 75%)
+7.922e+04
+1.500e+04
+1.250e+04
+1.000e+04
+7.500e+03
+5.000e+03
+2.500e+03
+0.000e+00
-2.500e+03
-5.000e+03
-7.500e+03
-1.000e+04
-1.250e+04
-1.500e+04
-5.426e+04
ODB: 10I.odb ABAQUS/STANDARD Version 6.6-1 Thu Oct 12 07:54:46 Eastern Daylight Time 2006
Step: Pressure, Pressure Load
Increment 1: Step Time = 1.000
Primary Var: S, S23
S, S23
(Avg: 75%)
+3.778e+04
+1.500e+04
+1.250e+04
+1.000e+04
+7.500e+03
+5.000e+03
+2.500e+03
+0.000e+00
-2.500e+03
-5.000e+03
-7.500e+03
-1.000e+04
-1.250e+04
-1.500e+04
-2.361e+04
ODB: 10Kweak.odb ABAQUS/STANDARD Version 6.6-1 Thu Oct 12 14:20:33 Eastern Daylight Time 2006
Step: Pressure, Pressure Load
Increment 1: Step Time = 1.000
Primary Var: S, S23

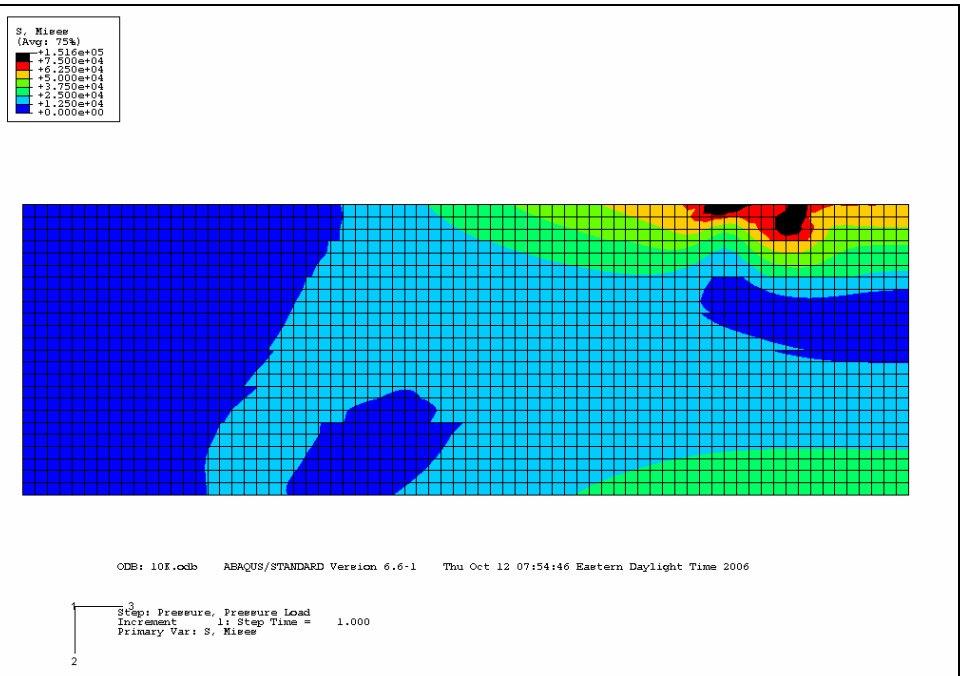
S, Mises
(Avg: 75%)
+1.516e+05
+7.500e+04
+6.250e+04
+5.000e+04
+3.750e+04
+2.500e+04
+1.250e+04
+0.000e+00
ODB: 10K.odb ABAQUS/STANDARD Version 6.6-1 Thu Oct 12 07:54:46 Eastern Daylight Time 2006
Step: Pressure, Pressure Load
Increment 1: Step Time = 1.000
Primary Var: S, Mises

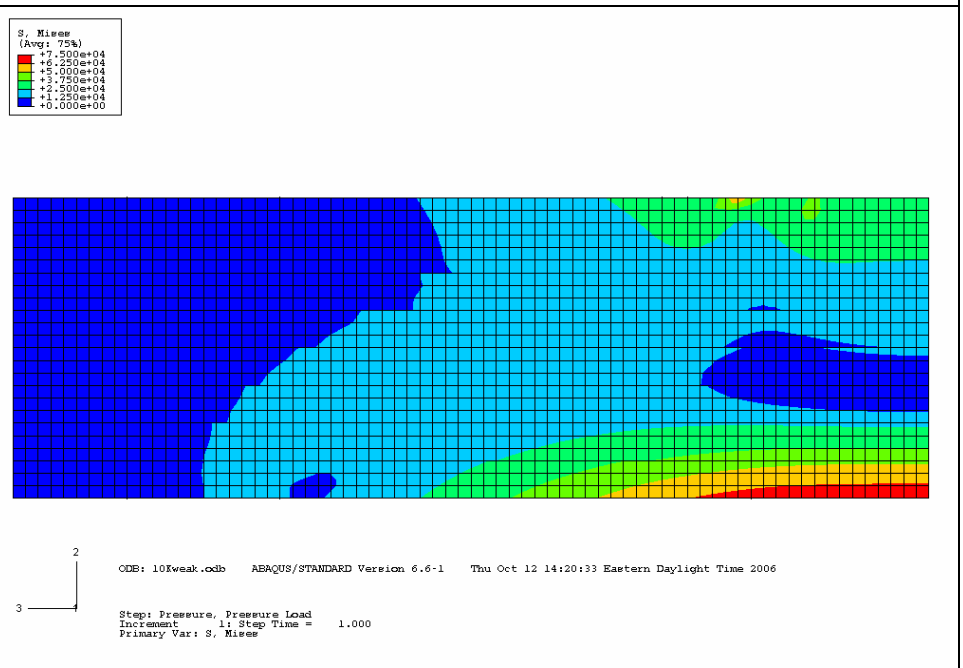
S, Mises
(Avg: 75%)
+7.500e+04
+6.250e+04
+5.000e+04
+3.750e+04
+2.500e+04
+1.250e+04
+0.000e+00
ODB: 10Kweak.odb ABAQUS/STANDARD Version 6.6-1 Thu Oct 12 14:20:33 Eastern Daylight Time 2006
Step: Pressure, Pressure Load
Increment 1: Step Time = 1.000
Primary Var: S, Mises

VITA

Mr. Robert Reuter graduated from Beavercreek H.S., Beavercreek, OH in May 1997. Past high school, Mr. Reuter earned a B.S. in materials science at Wright State University in Dayton, OH in the Spring of 2002. He worked previously in AFRL's Materials Laboratory in the metals fatigue branch (MLMMN) and then in the polymers branch (MLBP) as a student. Also, he gained experience interning at Wright State University under the tutelage of Dr. Maher Amer and at the National Composite Center (NCC) as a business intern. Mr. Reuter is currently employed by the United States Air Force Air Vehicles Directorate (AFRL/VASM) as an aerospace engineer. And very soon he will be a proud father.

BIBLIOGRAPHY

Erdogan, F. *Fracture Mechanics of Functionally Graded Materials*. F49620-93-1-0252. Bethlehem PA: Lehigh University, October 1996.
(ADA326172).

Gu, Pei, and R.J. Asara. "Crack Deflection in Functionally Graded Materials," *Int. J. Solid Structures*, Vol 34, No 24, pp. 30085-3098, 1997.

J.N. Reddy. "Analysis of Functionally Graded Plates," *International Journal for Numerical Methods in Engineering*, Vol 47, 663-684 (2000).

Yang J., and H.-S Shen, "Vibration Characteristics and Transient Response of Shear-Deformable Functionally Graded Plates in Thermal Environments," *Journal of Sound and Vibration*, Vol 255 No 3, 579-602 (2000).

Rodriguez-Castro, R, R.C. Wetherhold, and M.H. Kelestemur, "Microstructure and Mechanical Behavior of Functionally Graded Al A359/SiCp Composite," *Materials Science and Engineering*, A323:445-456 (2002).

Atri, R.R., and K.S. Ravichandran, and S.K. Jha, "Elastic Properties of In-Situ Processed Ti-TiB composites measured by impulse excitation of vibration," Materials Science and Engineering A. Vol 271, Issues 1-2, 150-159 (November 1999).

Ma J., and G.E.B. Tan, "Processing and Characterization of Metal-Ceramics Functionally Gradient Materials," *Journal of Materials Processing Technology*, 113: 446-449 (2001).

Lecompte, D., et. al, "Analysis of Speckle Patterns for Deformation Measurements By Digital Image Correlation," Proceedings of SPIE Vol 6341, 6431E (2006).

Mencik, Jaroslaw. *Strength and Fracture of Glass and Ceramics*. Amsterdam: Elsevier, 1992, p 227-234.

Panda, K.B., and K.S. Ravi Chandran. "Titanium-Titanium Boride (Ti-TiB) Functionally Graded Materials through Reaction Sintering: Synthesis, Microstructure, and Properties," *Metallurgical and Materials Transactions*, Vol 34A (September 2003).

Sekhar, Soma, et. al., "Cohesive modeling of dynamic fracture in functionally graded materials," *International Journal of Fatigue*, 132:275-296 (Spring 2005).

Cleland, John, and Francesco Iannetti, "Thermal Protection System of the Space Shuttle," NASA Report CR-4227. Research Triangle Park, NC: Research Triangle Institute.

National Aeronautics and Space Administration, "NASA Facts," FS-2000-06-29-KSC. Kennedy Space Center Florida: John F. Kennedy Space Center (1997).

The Flight Capable Distributed Sensing System. User's Manual Revision 4.0. Blacksburg VA: Luna Innovations, Inc.

Wallace, Colin G., Andreas Othonos, and Deepak Uttamchandani, "Fibre Bragg Grating Based Laser Sensor," SPIE Vol 2509, 48-56.

Thermal Imaging, Thermal NDE, and Thermoelastic Stress Analysis System. DeltaTherm Instruction Manual. Madison WI: Stress Photonics, Inc.

Lesniak, Jon K and Bradley R. Boyce, "Differential Thermography Applied to Stuctural Integrity Assessment," SPIE Vol 2473, 179-189.

Kaplan, Herbert and Paul Zayicek, "An Application of Differential Thermography in Power Generation Facilities," SPIE Vol 2473, 67-74.

Erdogan, Fazil, and Tz-Cheng Chiu, "Buckling of Graded Coatings: A Continuum Model," Lehigh University Mechanical Engineering and Mechanics. Bethlehem, PA (2000).

Rodriquez-Castro, R., R.C. Wetherhold, and M. H. Kelestemur, "Microstructure and Mechanical Behavior of Functionally Graded Al A359/SiCp Composite," Materials Science and Engineering. A323, 445-456 (2002).

"Finite Element Analysis." Excerpt from unpublished article. n. pag. http://en.wikipedia.org/wiki/Finite_element_analysis. 26 October 2006.

Beckwith, T.G., and N. Lewis Buck. *Mechanical Measurements*. Phillipines: Addison-Wesley, 1973.

Erdogan F., and B.H. Wu, *Crack Problems in FGM Layers Under Thermal Stresses.* AFOSR Contract F49620-93-1-0252. Bethlehem PA: Lehigh University, October 1995.

Jackson, Melvin R., *Polycomponent Functionally Graded Materials for Thermal Barrier Systems.* Contract: F49620-95-C-0028. Washington DC: Bolling AFB.

Feng, H.-B., D.-C. Jia, Y. Zhou, and J Huo, "Microstructural Characterisation of *in situ* TiB/Ti matrix composites prepared by mechanical alloying and hot pressing," *Materials Science and Technology*, Vol 20, September 2004.

Diefendorf, R.J., J.G. Goree, M. Graujicic, and P.F. Joseph, *Design, Analysis, and Processing of Functionally Graded Structural Materials – Final Report.* Contract: ARO 35814.26-MS-DPS. Clemnson SC: Clemson University.

Assao, R.J., Deformation and Failure in Functionally Graded Materials. Grant No: N00014-93-1-1164. San Diego CA: The Regents of the University of California.

Erdogan, Fazil, and Maheendra Kasmalkar, *The Suface Crack Problem for a Functionally Graded Coating Bonded to a Homogenous Layer.* Contract: F49620-98-1-0028. Bethlehem PA: Lehigh University.

Reimanis, Ivar, and John Berger, The Role of Interfaces in the Fractur of Functionally Graded Materials. Contract: DAAD19-010-1-0590. Golden CO; Colorado Center for Advanced Ceramics.

Reddy, J. N., "Analysis of Functionally Graded Plates," *International Journal for Numerical Methods in Engineering*, 47: 663-684 (2000).

Nakamura, Toshio. *Optimizing Functionally Graded Materials to Resist Failure under Dynamic Loadings.* Contract: DAAD19-99-1-0318. Stony Brook NY: The Research Foundation of SUNY Office of Sponsored Programs.

Venkataraman, Satchi, and Bhavani V. Sankar, Analysis of Sandwich Beams with Functionally Grade Core. Contract: NAG-1-1887. Gainesville FL: University of Florida.

Nakamura, T., T. Wang, and S. Sampath, "Determination of Properties of Graded Materials by Inverse Analysis and Instrumented Indentation," Acta Materialia. 48: 4293-4306 (2000).

Love, B.M. and R.C. Batra, Localization of Deformation in Heterogeneous Solids Deformed at High Strain Rates. Contract: DAAD19-01-0657. Blacksburg VA: Virginia Polytechnic University.

Tippur, Hareesh V., *Crack Tip Fields Mapping and Failure Characterizataion of Functionally Graded Composites*. Contract: DAAG55-97-0110. Auburn AL: Auburn University.

Boyer, Rodney, Gerhard Welsch, and E.W. Collings, eds. Materials Properties Handbook: Titanium Alloys. ASM International: 1994. p. 179

Davis, Joseph, ed. *Properties and Selection: Nonferrous Alloys and Special-Purpose Materials. ASTM Metals Handbook Volume 2*: 1990. p. 1169

Air Force Research Laboratory Homepage. http://www.afrl.af.mil/, 10 January 2006.

Hill, M.R., and Lin, Wei-Yan, "Residual Stress Measurement in a Ceramic-Metallic Graded Material", J. of Eng. Mat. And Tech., April 2002, Vol. 124, pp. 185-191.

http://www.sv.vt.edu/classes/MSE2094_NoteBook/97ClassProj/exper/halahan/www/halahan.html

REPORT DOCUMENTATION PAGE

Form Approved OMB No. 074-0188

1. REPORT DATE *(DD-MM-YYYY)*	2. REPORT TYPE	3. DATES COVERED *(From – To)*
21 Dec 06	Master's Thesis	Jun 2003 – Dec 2006

4. TITLE AND SUBTITLE

An Exploration of Several Structural Measurement Techniques for Usage with Functionally Graded Materials

5a. CONTRACT NUMBER

5b. GRANT NUMBER

5c. PROGRAM ELEMENT NUMBER

6. AUTHOR(S)

Reuter, Robert

5d. PROJECT NUMBER

5e. TASK NUMBER

5f. WORK UNIT NUMBER

7. PERFORMING ORGANIZATION NAMES(S) AND ADDRESS(S)
Air Force Institute of Technology
Graduate School of Engineering and Management (AFIT/EN)
2950 Hobson Way
WPAFB OH 45433-7765

8. PERFORMING ORGANIZATION REPORT NUMBER

AFIT/GAE/ENY/07-D03

9. SPONSORING/MONITORING AGENCY NAME(S) AND ADDRESS(ES)
AFRL/VASM
Attn: Dr. Eric Tuegel
2790 D. St. Bldg 65
WPAFB OH 45433

10. SPONSOR/MONITOR'S ACRONYM(S)
AFRL/VASM

11. SPONSOR/MONITOR'S REPORT NUMBER(S)

12. DISTRIBUTION/AVAILABILITY STATEMENT
APPROVED FOR PUBLIC RELEASE; DISTRIBUTION UNLIMITED.

13. SUPPLEMENTARY NOTES

14. ABSTRACT

Titanium / titanium boride functionally graded 6"x1"x1" beams were subjected to a four-point beam test in order to critique the value of several measurement techniques. Also, finite element analysis results were compared with experimental values and general observations about the experiment were recorded. Uniform 85% TiB / 15% Ti and uniform commercially pure titanium specimens were also subjected to the same loading conditions as a control. Techniques used include digital image correlation, fiber optic strain gauging, strain gauging, and differential infrared thermography techniques. The strain data results were compared with one another and to linear finite element models. It was found that several of the techniques had distinct advantages and disadvantages for usage in a layered functionally graded system. Furthermore, the finite element showed good agreement with results when overlaid with several of the measurement techniques.

15. SUBJECT TERMS
Differential Thermography, Digital Image Correlation, Fiber-Bragg Gratings, Ti-TiB, Functionally Graded Materials, Bending

16. SECURITY CLASSIFICATION OF:			17. LIMITATION OF ABSTRACT	18. NUMBER OF PAGES	19a. NAME OF RESPONSIBLE PERSON
REPORT	ABSTRACT	c. THIS PAGE			Dr. Marina Ruggles-Wrenn
U	U	U	UU	71	19b. TELEPHONE NUMBER *(Include area code)* (937) 255-6565, ext 4641